Acta Astronautica 247 (2026) 743–764

Contents lists available at ScienceDirect

Acta Astronautica

journal homepage: www.elsevier.com/locate/actaastro

A comparative assessment of heliocentric and controlled lunar impact end-of-life disposal strategies for Near Rectilinear Halo Orbits☆

Mathilda Bolis [a,*], Elisa Maria Alessi [b], Camilla Colombo [a]

[a] Dipartimento di Scienze e Tecnologie Aerospaziali (DAER), Politecnico di Milano, Via La Masa, 34, Milano, 20156, Italy
[b] Istituto di Matematica Applicata e Tecnologie Informatiche "Enrico Magenes", Consiglio Nazionale delle Ricerche, Via Alfonso Corti 12, Milano, 20133, Italy

ARTICLE INFO

Keywords:
Cislunar space
Heliocentric disposal
Controlled lunar impact
Near Rectilinear Halo Orbits
Cislunar Space Situational Awareness

ABSTRACT

In the coming decades, space traffic within the cislunar region is expected to grow exponentially, driven by an increasing number of planned missions to the Moon and related studies. Since severe issues with the management of man-made space debris have already been observed in near-Earth orbits, it is crucial to address this problem proactively to prevent a similar situation from developing in the cislunar region. This is particularly relevant given that managing debris in the cislunar environment would be considerably more challenging than in near-Earth orbits, due to the greater distance from Earth and the inherently nonlinear and chaotic dynamics that characterise cislunar space. The most effective approach to address these issues would be to incorporate mitigation measures directly into the mission design phase, for instance, carefully planning a priori low-cost, robust End-of-Life (EoL) disposal phases, particularly for spacecraft orbiting in regions expected to host a significant proportion of future space traffic. In this scenario, a key role is played by Near Rectilinear Halo Orbits (NRHOs), which are considered highly attractive candidates for future missions. Of the four main EoL disposal strategies available in the Earth–Moon (EM) system, two are particularly well-suited to spacecraft operating in NRHOs: heliocentric disposal and controlled lunar impact. The first relies on injecting the spacecraft onto the unstable manifold of the reference periodic orbit, allowing the trajectory to leave the EM vicinity passing through EM-L_2, for then, with appropriate phasing between the EM and Sun–Earth (SE) systems, transit through either SE-L_1 or L_2. To prevent re-entry into the Earth's neighbourhood, the SE Zero-Velocity Curves (ZVCs) should then be closed to ensure a no-return escape. On the other hand, controlled lunar impact can be defined as an optimisation problem. After inserting the spacecraft on the unstable manifold, small manoeuvres are introduced to target Moon impact while ensuring that historical sites and protected regions are avoided. The results obtained are then refined using an ephemeris-based dynamical model. These two disposal strategies are applied to six cislunar Lagrangian Point Orbits (LPOs): 4 NRHOs, two in EM-L_1 and two in EM-L_2, and 2 Halo orbits, one in EM-L_1 and one in EM-L_2. The results obtained are then compared in terms of ΔV, Time of Flight (ToF), and robustness. This work aims to provide a preliminary overview of disposal design for EM–NRHOs, including an assessment of the dynamical mechanisms that govern such disposal strategies.

1. Introduction

Cislunar space is a region strongly influenced by the combined gravitational fields of the Earth and Moon. It is typically defined as extending from the hyper-geostationary area to the Earth–Moon (EM) Lagrangian points [1], and it is of significant interest for future exploration. Not only does it represent the first frontier of space beyond the near-Earth environment that humanity can access, but it could also serve as a critical link between the Earth and more distant regions of space. Numerous missions are expected to reach this area in the near future, ranging from large-scale programmes such as NASA's Artemis mission [2], to smaller science-focused exploration CubeSats. Nevertheless, operating in cislunar space is challenging due to its intrinsic nonlinear dynamics, of which many aspects are still insufficiently explored for complete characterisation, and the great distance from Earth, which increases operational and observational complexity.

In parallel with the growing interest directed towards the cislunar region, international awareness of the space debris problem has also

☆ This article is part of a Special issue entitled: '76th IAC_invited only' published in Acta Astronautica.

* Corresponding author.
E-mail addresses: mathilda.bolis@polimi.it (M. Bolis), elisamaria.alessi@cnr.it (E.M. Alessi), camilla.colombo@polimi.it (C. Colombo).

https://doi.org/10.1016/j.actaastro.2026.05.039
Received 28 February 2026; Received in revised form 4 May 2026; Accepted 20 May 2026
Available online 26 May 2026

increased significantly in recent years. Various institutions are beginning to recognise space as a finite environmental resource, the use of which must be carefully regulated, like any Earth-based ecosystem. The rapid growth in the number of launches and in the population of space objects, both controlled and uncontrolled, orbiting in the near-Earth region has already led to an exponential rise in the number of close encounters, posing risks to current and future missions [3]. Given the number of satellites planned to operate in cislunar space in the coming years, it is essential to identify effective measures to prevent the rise of a similar debris problem in this region, where the consequences could be even more severe than those currently observed in near-Earth space. This can only be achieved by promoting mission architectures that are sustainable by design, integrating disposal, risk-reduction, and long-term environmental protection considerations directly within the mission design space. With this in mind, one of the most important aspects of designing a sustainable mission is undoubtedly ensuring that a spacecraft can be disposed of thoroughly at its End-of-Life (EoL).

In this work, two EoL disposal strategies are modelled and analysed with reference to a set of orbits of particular relevance as eventual operational options. Near-Rectilinear Halo Orbits (NRHOs) are members of the Halo family characterised by close proximity to the Moon and by higher linear stability compared to other types of Libration Point Orbits (LPOs), making them particularly attractive as candidates for future mission architectures. At the same time, NRHOs belong to a dynamical regime with peculiar characteristics even within the broader cislunar environment: the gravitational influence of the Moon is particularly strong, and the contributions of its higher-order gravitational harmonics and of the Sun's gravitational acceleration are not negligible.

Four main EoL disposal strategies can generally be applied to spacecraft in the EM system, according to ESA, "in order of preference: heliocentric disposal, lunar impact, Earth re-entry, or a lunar graveyard orbit" [4].

Once a disposal strategy has been designed, it is recommended that the resulting trajectory is validated through long-term propagation in an ephemeris-based dynamical model over a period of at least 100 years. Moreover, disposal strategies must not only comply with safety requirements to avoid interfering with current and future missions, but must also be adapted to the specific dynamic characteristics of the operational orbit in question. Given their geometric and dynamical characteristics, two disposal strategies are considered the most convenient for NRHOs: heliocentric and controlled lunar impact.

Heliocentric disposal was first studied for LPOs in the SE system in [5], and it is designed following a two-impulse trajectory escaping the Earth's neighbourhood. Given a certain location along an LPO in the EM system, identified in this work through the phase angle, an object is first inserted into its unstable manifold with a positive or negative perturbation. It then follows the manifold's natural dynamics first in the EM Circular Restricted Three-Body Problem (CR3BP), and then in the Sun–Earth (SE) CR3BP, once the influence of the Sun becomes dominant over that of the Moon, until eventually reaching the SE-L_1 or L_2 bottleneck. After passing through one of these, a second manoeuvre is performed, and the Zero Velocity Curves (ZVCs) of the SE system are closed with an energetic approach to prevent the spacecraft from re-entering the Earth's vicinity. This disposal strategy has been applied to the Herschel and Planck missions; it has also been proposed for SOHO and Gaia in [6], all operating in SE-LPOs; and again for the Gaia mission in [7]. As concerns NRHOs in EM-L_2, studies considering heliocentric escape as a promising disposal option for spacecraft operating in the reference orbit of the Lunar Gateway have been proposed in [8,9], although with some relevant variation in the design of the escape trajectories with respect to what has been developed in this work.

On the other hand, controlled lunar impact is approached as an optimisation problem. An initial perturbation, either positive or negative, is applied to an object in orbit on an EM-LPO in the direction of its unstable manifold. The satellite to be disposed of then follows the unstable manifold until it reaches a certain position, at which point an impulse is given in the velocity direction. This lowers the perilune of the orbit, resulting in an impact with the Moon after a maximum of three impulses, including the one applied in the unstable manifold direction. The objective is to minimise the total ΔV required to perform the procedure while imposing constraints on the maximum Time of Flight (ToF) and impact points. The first constraint prevents the spacecraft from spending too much time in a region characterised by strong nonlinear dynamics caused by the combined influence of the Moon's, Earth's and Sun's gravity, as well as that of the lunar gravitational harmonics. The second constraint aims to avoid impacting regions of historical significance, such as lunar missions heritage sites, as well as regions of strong interest for future exploration, such as those close to the lunar poles. Finally, the solutions obtained are refined preliminarily in an ephemeris-based dynamical model, considering the influence of the Sun, the Moon, the Earth's gravity and the lunar gravitational harmonics. Lunar impact was designed as a disposal option for the Gaia mission in [7]. Cislunar debris mitigation analyses have also been carried out in previous studies, although these were conducted mainly within an ephemeris-based dynamical framework, for example, in [10].

Both disposal options are applied to six LPOs: four NRHOs, two in EM-L_1 and two in L_2, and two Halo orbits close to the NRHO regime. The latter were included in the analyses for the purpose of a preliminary comparison between the behaviour of NRHOs during disposal and that of Halo orbits. The two disposal strategies are compared in terms of operational complexity, required ΔV and disposal time. Furthermore, a set of key parameters that are expected to have a significant impact on the outcome of the analysis has been identified and will be examined in greater detail in future works.

2. Dynamical modelling

Various dynamical models can be used to describe the motion of a particle orbiting in cislunar space, primarily influenced by the gravitational attraction of the Earth and the Moon, but also affected by other smaller effects. A dynamical model including them all yields the most accurate representation of the real environment. However, doing so increases the difficulty of isolating the contribution of individual perturbations and results in longer, more complex simulations. Approximate models, such as the CR3BP, account for only a subset of the forces acting on the particle, assuming the motion takes place in a region where specific effects predominate. Integrating such approximated models into preliminary analyses and subsequently validating the results within more complete dynamical frameworks can be an effective strategy, provided that conclusions are drawn while having in mind the assumptions under which such approximations remain valid. This Section presents the dynamical models used in the analyses conducted in this work, together with the corresponding relationships.

2.1. Circular restricted three body problem

The CR3BP [11] is a simplified dynamical model widely employed to describe the motion of a particle within a region of space dominated by the strong gravitational influence of two major primaries. In this study, it is adopted as the reference dynamical framework, where the two primary bodies are, respectively, the Earth and the Moon (EM-CR3BP) or the Sun and the EM system (SE-CR3BP). The third body is assumed to have a negligible mass and represents the satellite. The orbits of the two primaries are assumed circular, revolving about their common centre of mass with a constant angular velocity. The reference frame associated with the model is a rotating one, centred at the system barycentre, with the Equations of Motion (EoMs) formulated in a non-dimensional form. The CR3BP EoMs are defined such that:

$$\begin{cases} \dot{\boldsymbol{r}} = \boldsymbol{v} \\ \dot{\boldsymbol{v}} = 2\begin{bmatrix} v_y \\ -v_x \\ 0 \end{bmatrix} + \nabla_{\boldsymbol{r}} U(\boldsymbol{r}) \end{cases} \tag{1}$$

where the potential-like function U is defined as:

$$U(\boldsymbol{r}) = \frac{1}{2}(r_x^2 + r_y^2) + \frac{1-\mu}{r_1} + \frac{\mu}{r_2} + \frac{1}{2}\mu(1-\mu) \tag{2}$$

In this formulation, the parameter μ denotes the dimensionless gravitational constant related to the coupling of the two primaries of the system. Its value is 0.01215 for the EM-CR3BP, and 3.0404×10^{-6} for the SE system. The variables r_1 and r_2 represent the distances between the third body and the two primaries, respectively. In the adopted reference frame, the larger primary is located at $x = -\mu$, while the smaller primary is located at $x = 1-\mu$. Accordingly, r_1 and r_2 can be expressed as:

$$r_1 = ((r_x + \mu)^2 + r_y^2 + r_z^2)^{1/2} \tag{3}$$

$$r_2 = ((r_x - 1 + \mu)^2 + r_y^2 + r_z^2)^{1/2} \tag{4}$$

Lengths are scaled with respect to the mean EM or SE distance, depending on the system under analysis, while time is scaled such that the mean angular velocity of the rotating frame is equal to 1. Dimensionless lengths are expressed in units of LU, standing for Length Unit (LU), and dimensionless time is expressed in units of TU, Time Unit (LU). Within the CR3BP framework, only one integral of motion exists, known as the Jacobi Constant (JC), and given by:

$$JC(\boldsymbol{r}, \boldsymbol{v}) = 2\bar{U}(\boldsymbol{r}) - \|\boldsymbol{v}\|^2 \tag{5}$$

where $\bar{U}(\boldsymbol{r})$ denotes the potential function $U(\boldsymbol{r})$ with the constant term removed. According to this definition, an increase in the JC corresponds to a decrease in the total energy of the system, and vice versa. Within the CR3BP framework, five equilibrium points, commonly referred to as the libration or Lagrange points L_1 through L_5, can be identified, along with families of periodic and quasi-periodic solutions. The JC serves as a reference parameter for classifying the states accessible to a particle from a dynamical point of view, particularly those related to the previously mentioned equilibrium points and families of periodic orbits. In the spatial CR3BP, for a given value of the JC, denoted JC_0, the dynamics is constrained to a five-dimensional energy surface embedded within the six-dimensional phase space. The regions accessible to a massless particle with JC equal to JC_0 in a system characterised by the gravitational parameter μ are obtained by projecting this energy surface onto the configuration space of the rotating reference frame. These regions are traditionally known as Hill regions, whose boundaries, referred to as Zero Velocity Curves (ZVCs), correspond to locations where the kinetic energy of the massless particle is zero, thus defining the limits of its possible motion. The ZVCs of the SE system in the Earth neighbourhood are shown on the left-hand side of Fig. 1 as a function of various JCs in the SE system. On the right-hand side of the same figure, the Hill regions of the SE system evaluated at the JC corresponding to SE–L_2 are reported.

2.2. Coupled circular restricted three body problem

In this work, the coupled CR3BP framework is adopted to describe the motion of a particle governed first by the EM-CR3BP and subsequently by the SE-CR3BP. An alternative dynamical model, which describes a similar scenario, is the Bicircular Restricted Four-Body Problem (BR4BP), i.e., [12]. In the present analysis, however, the coupled CR3BP is preferred, as it allows full decoupling of the Sun's influence from that of the Moon, a characteristic that will be useful for representing clearly some behaviours of interest.

The coupled CR3BP model adopted in this context is based on the assumption that the SE and EM systems are coplanar, with the Moon's orbit assumed to lie in the ecliptic plane, and that the EM-CR3BP approximation remains valid as long as the influence of the Sun on the system does not exceed that of the Moon, and vice versa. Although the approximation that all three primary bodies lie in the same orbital plane affects the results, it significantly simplifies the formulation by requiring only a single angular parameter, rather than two, to define the relative orientation of the two rotating reference frames.

A point mass in the EM system, initially located in the vicinity of the Moon, is propagated using the EM-CR3BP dynamics until a specified threshold is reached, at which point the dynamical model switches to the SE-CR3BP. The formulation proposed in [13] is adopted: the transition from the EM to the SE-CR3BP occurs when, if modelled within the BR4BP framework, the effect of the Moon becomes negligible compared to that of the Sun on the trajectory. Vice versa, for transitions from the SE-CR3BP back to the EM-CR3BP, it is determined when the Sun's influence becomes negligible compared to that of the Moon. The two dynamical models are connected through a coordinate transformation, defined based on the geometry of the system, schematically represented in Fig. 2, where the subscript in indicates a generic inertial frame, SE refers to the SE rotating reference frame and EM to the EM rotating one.

The angle α, defined as the difference between α_m and α_s is used to compute the geometric relationships between the two rotating systems, knowing that:

$$\alpha = \alpha_0 + \frac{\omega_{EM} - \omega_{SE}}{\omega_{EM}} t_{EM} \tag{6}$$

defines the evolution of the angle α in the EM system, being ω_{EM} and ω_{SE} the non-dimensional angular velocities of the two rotating frames, respectively; t_{EM} the non-dimensional time in the EM system at which α has to be computed; and α_0 the initial value of α, evaluated at the generic initial time t_0. Using complex notation, to convert a position in the EM system to one in the SE:

$$\begin{cases} \boldsymbol{b_{SE}} = \dfrac{l_{EM}}{l_{SE}} e^{i\alpha} \boldsymbol{b_{EM}} + 1 - \mu_{SE} \\ r_{z_{SE}} = \dfrac{l_{EM}}{l_{SE}} r_{z_{EM}} \end{cases} \tag{7}$$

where

$$\boldsymbol{b_{SE}} = r_{x_{SE}} + i\, r_{y_{SE}} \qquad \boldsymbol{b_{EM}} = r_{x_{EM}} + i\, r_{y_{EM}} \tag{8}$$

and l_{EM} and l_{SE} are respectively the characteristic lengths of the EM and SE systems. To transform a velocity vector from the EM to the SE system:

$$\begin{cases} \dot{\boldsymbol{b}}_{\boldsymbol{SE}} = \dfrac{l_{EM}}{l_{SE}} \dfrac{\omega_{EM}}{\omega_{SE}} e^{i\alpha} \left(i \left(1 - \dfrac{\omega_{SE}}{\omega_{EM}} \right) \cdot \boldsymbol{b_{EM}} + \dot{\boldsymbol{b}}_{\boldsymbol{EM}} \right) \\ v_{z_{SE}} = \dfrac{l_{EM}}{l_{SE}} \dfrac{\omega_{EM}}{\omega_{SE}} v_{z_{EM}} \end{cases} \tag{9}$$

where

$$\dot{\boldsymbol{b}}_{\boldsymbol{SE}} = v_{x_{SE}} + i\, v_{y_{SE}} \qquad \dot{\boldsymbol{b}}_{\boldsymbol{EM}} = v_{x_{EM}} + i\, v_{y_{EM}} \tag{10}$$

To perform the inverse transformation (from SE to EM), it is sufficient to invert the equations.

It is important to note that both the EM and SE-CR3BP are autonomous dynamical models, i.e., their dynamics do not explicitly depend on time. However, the transformation from one system to the other depends on the angle α, which is a function of the initial relative configuration of the Sun–Earth–Moon system and could also be interpreted as a function of time. Consequently, the epoch at which the spacecraft propagation begins, expressed in terms of the initial value α_0, is a key parameter in the definition of the outcomes of an analysis performed in the coupled CR3BP dynamical model.

2.3. Ephemeris-based dynamical model and lunar gravitational harmonics

The CR3BP is a reasonable approximation of the dynamics of a particle in cislunar space, where the coupled EM gravitational influence is prevalent. However, this approximation becomes less representative of the true, non-approximated dynamics of an object entering regions of space where additional effects are no longer negligible, such as

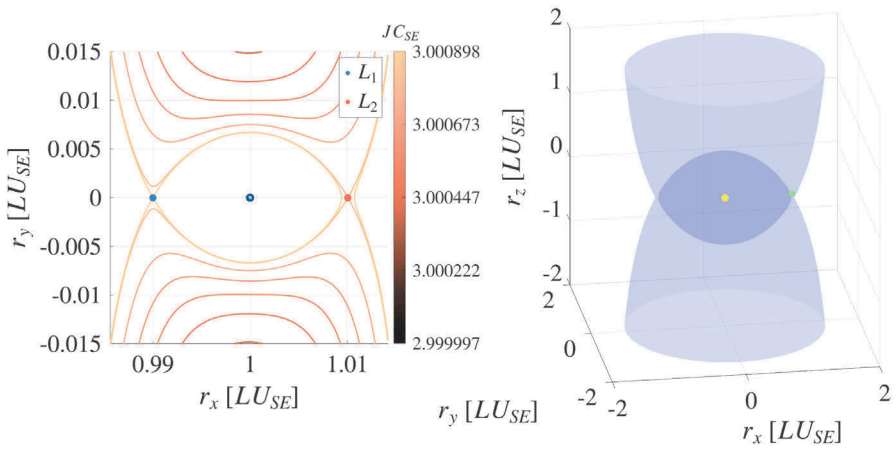

Fig. 1. Left: ZVCs of the SE system in the Earth's neighbourhood as a function of JC_{SE}. SE-L_1 and L_2 are represented by a blue and a red dot, respectively. The Earth, shown at the centre of the plot, is scaled to be ten times its actual size for visualisation. Right: Hill regions in the SE system, evaluated for a JC_{SE} equal to that of SE-L_2. The EM centre of mass and the Sun are represented by a green and a yellow dot, respectively. (For interpretation of the references to colour in this figure legend, the reader is referred to the web version of this article.)

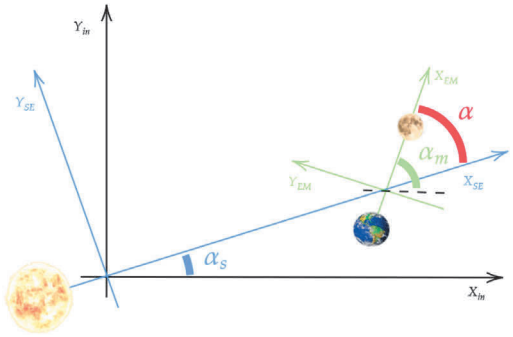

Fig. 2. Approximation considered to model the relationship between the SE and the EM rotating frame.

the influence of high-order lunar gravitational harmonics when in the vicinity of the lunar surface. Using the coupled CR3BP dynamical model, it is possible to reasonably approximate the motion of a particle that is initially governed by the EM-CR3BP and subsequently by the SE-CR3BP, i.e., a particle escaping the EM system. Instead, when designing lunar-impact trajectories, an ephemeris-based model should be used to refine the solutions initially obtained within the CR3BP framework to account for the effects of lunar gravitational harmonics and the Sun's gravitational influence in the disposal design. Knowing the state of a particle in the EM-CR3BP, it is first necessary to express it in a reference frame coherent with an ephemeris-based dynamics: to do so, the Moon-centred J2000 inertial reference frame is chosen. To perform the coordinate transformation, a strategy similar to that described in [14], and later also presented in works such as [15], is adopted, but adapted to the specific case in which the transformation must map the EM rotating reference frame to the Moon-centred J2000 frame, and vice versa. Let $\boldsymbol{r}$ be the position of a point in the EM rotating reference frame and $\hat{\boldsymbol{r}}$ that same position in the Moon-centred J2000 frame. It is possible to state that [14]:

$$\hat{\boldsymbol{r}} = k\boldsymbol{C}\boldsymbol{r} + \boldsymbol{b} \tag{11}$$

where $k = \|\boldsymbol{R_M} - \boldsymbol{R_E}\|$ is a scaling factor, with $\boldsymbol{R_M}$ and $\boldsymbol{R_M}$ being the position of the Moon and the Earth, respectively, in the J2000 frame centred at the EM barycentre, computed via the DE440 kernel of the NASA SPICE [16] toolkit. The vector $\boldsymbol{b}$ shifts the centre of the system from the EM barycentre to the Moon, and the matrix $\boldsymbol{C}$ is an orthonormal matrix representing the rotation from the EM rotating to the inertial frame:

$$\boldsymbol{c_1} = \frac{\boldsymbol{R}}{k} \qquad \boldsymbol{c_3} = \frac{\boldsymbol{R}\times\boldsymbol{V}}{\|\boldsymbol{R}\times\boldsymbol{V}\|} \qquad \boldsymbol{c_2} = \boldsymbol{c_3}\times\boldsymbol{c_1} \tag{12}$$

where $\boldsymbol{R} = \boldsymbol{R_M} - \boldsymbol{R_E}$ and $\boldsymbol{V} = \boldsymbol{V_M} - \boldsymbol{V_E}$. The relation between the velocity in the EM rotating frame, $\boldsymbol{v}$, and that in the Moon-centred J2000 frame, $\hat{\boldsymbol{v}}$, can be found as the derivative with respect to time of Eq. (11). It is important to note that the transformation is ephemeris-based, i.e., it is time-dependent, and accounts for the roto-pulsating effects arising both from the rotation of the EM reference frame with respect to the inertial one and from the time-varying distance between the Earth and the Moon. Once the spacecraft state has been retrieved in the Moon-centred J2000 frame, the EoMs of the ephemeris-based dynamics can be expressed as follows:

$$\begin{cases} \dot{\hat{\boldsymbol{r}}} = \hat{\boldsymbol{v}} \\ \dot{\hat{\boldsymbol{v}}} = -\mu_M \dfrac{\hat{\boldsymbol{r}}}{\|\hat{\boldsymbol{r}}\|^3} + \hat{\boldsymbol{a}}_p \end{cases} \tag{13}$$

where μ_M is the standard gravitational constant of the Moon. The vector $\boldsymbol{a_p}$ represents the sum of the perturbing accelerations to which the spacecraft is subject due to the third-body gravitational influence of both the Sun and the Earth, and to the presence of the lunar gravitational harmonics. Consequently, it is given $\hat{\boldsymbol{a}}_p = \hat{\boldsymbol{a}}_{3b_E} + \hat{\boldsymbol{a}}_{3b_S} + \hat{\boldsymbol{a}}_G$, where:

$$\hat{\boldsymbol{a}}_{3b_j} = \mu_j \left(\frac{\hat{\boldsymbol{r}}_{sc/j}}{\|\hat{\boldsymbol{r}}_{sc/j}\|^3} - \frac{\boldsymbol{R}_{j/M}}{\|\boldsymbol{R}_{j/M}\|^3} \right) \tag{14}$$

is the acceleration associated with the third-body perturbation exerted by the jth body, characterised by the μ_j gravitational coefficient, on the trajectory; $\boldsymbol{r}_{sc/j}$ denotes the position of the spacecraft with respect to the jth body; and $\boldsymbol{r}_{j/M}$ denotes the position of the jth body with respect to the Moon.

The perturbing acceleration $\hat{\boldsymbol{a}}_G$ is related to the lunar gravitational harmonics, and is computed, in a body fixed reference frame, as derived in [17] and later described in [18]. The formulation is based on the definition of the gravity potential, which may be written as:

$$U_g = \frac{GM_M}{R_M} \sum_{n=0}^{\infty} \sum_{m=0}^{n} (C_{nm} V_{nm} + S_{nm} W_{nm}) \tag{15}$$

where M_M and R_M are respectively the Moon's mass and radius; G is the universal gravitational constant; and the coefficients C_{nm} and S_{nm}, which relate the lunar gravitational potential to the Moon's internal mass distribution, are derived from data collected by the GRAIL

mission [19]. In this work, coefficients are included up to degree and order 50, which offers a sufficiently accurate representation of the real lunar dynamics. The quantities V_{nm} and W_{nm} satisfy specific recurrence relations, derived from the connections between the Legendre polynomials and the trigonometric functions appearing in the classical formulation of a planetary gravitational potential. Note that, following Eq. (15), the perturbing acceleration $\boldsymbol{a}_G$ is computed in a Moon-fixed reference frame, which is the same frame in which the lunar gravitational coefficients are defined, namely the Moon's Principal Axis (PA) frame, oriented as the Moon's principal inertia axes. To incorporate the effect of the lunar gravitational harmonics into the equations of motion expressed by Eq. (13), this acceleration must be rotated into the Moon-centred J2000 reference frame. The rotation matrix that transforms vectors from the PA frame to the Moon-centred J2000 frame can be retrieved at the appropriate ephemeris time using the *cspice_pxform* SPICE routine.

3. Periodic orbits candidates for the analysis

In this work, a total of six periodic orbits are selected for analysis: two NRHOs and a Halo orbit around EM-L_1, and two NRHOs and a Halo orbit around EM-L_2. Following the formulation in [12], each orbit is designed in the EM-CR3BP to satisfy symmetry about the xz-plane of the EM rotating reference frame, crossing this plane orthogonally, and to reproduce a given initial state exactly after one well-defined period. Starting from an initial guess, a differential correction algorithm is used to adjust the initial state vector until the desired periodic conditions are met. Among the various periodic orbits existing in the cislunar environment, NRHOs belong to a branch of the Halo family exhibiting an almost "near-linear" geometry, with a very high apolune and low perilune. These orbits are also characterised by a higher linear stability with respect to other members of the Halo family, as quantified by the Stability Index (SI). The SI is computed knowing that the six eigenvalues of the monodromy matrix, i.e., the state transition matrix evaluated over one orbital period, can be divided into three pairs: the first is trivial and equal to 1; the second consists of two complex conjugate numbers; and the last is given by a real number with modulus greater than 1 and its reciprocal. Considering only λ_{max}, the maximum eigenvalue of the monodromy matrix, belonging to the last pair, the SI can be computed as [20]:

$$SI = \frac{1}{2}\left|\left(\lambda_{max} + \frac{1}{\lambda_{max}}\right)\right| \tag{16}$$

The SI is a measure of linear stability, and a periodic orbit is classified as linearly stable when $SI \leq 1$ [21]. Note that this definition is given because trivial eigenvalues are not excluded from the computation of the SI in this case. NRHOs exhibit SI values that fall within the stable or unstable regime, yet remain very close to unity. Moreover, the maximum eigenvalues of unstable NRHOs' monodromy matrices are consistently negative, in contrast to what is observed for other unstable orbits belonging to the Halos family. It is important to note that no universally accepted criteria exist to unambiguously determine which are the boundaries of the NRHO range inside the Halo family. However, in this context, all orbits exhibiting these specific characteristics are considered to be NRHOs. In Fig. 3, the behaviour of the SI and of the maximum eigenvalue of the monodromy matrix, λ_{max}, is shown as a function of the perilune radius, i.e., the minimum distance between the orbit and the Moon, for a subset of orbits belonging to the NRHO regime in L_2 (left side of the graph) and L_1 (right side of the graph) or close by.

All unstable orbits that can be identified as NRHOs are located in the area highlighted in red, while linearly stable NRHOs are located in the light blue one. Due to their proximity to the Moon and distinctive characteristics, NRHOs are excellent candidates for a wide range of mission concepts and operational applications, and it is therefore of particular importance to study effective EoL disposal strategies for satellites operating in these types of orbits. This work only considers the southern branch of the Halo families, but similar results can be expected for the northern branch. The characteristics of the six periodic orbits for which disposal strategies are analysed are reported in Table 1, their detailed initial conditions in Appendix.

Table 1
Characteristics of the periodic orbits candidates for the analysis: JC, SI and r_p, perilune radius.

Orbit type	Id	JC [−]	SI [−]	r_p [km]
NRHO in EM-L_2	A2	3.0465	1.3223	3262.99
	B2	3.0279	1.6927	7627.33
Halo in EM-L_2	C2	3.0278	16.4465	27 468.05
NRHO in EM-L_1	A1	2.9979	2.6541	3219.67
	B1	3.0040	2.3274	6542.96
Halo in EM-L_1	C1	3.0043	8.0204	27 343.43

These same orbits are shown in Fig. 4 as a function of the phase angle, which represents a rescaling of the time required to reach a certain state along the periodic orbit. The phase angle is defined as:

$$\theta = 2\pi \frac{\hat{t}}{T} \tag{17}$$

where $\hat{t}$ is the time needed for a particle moving along the orbit to reach a certain state and T is the LPO period in the EM rotating frame. The phase angle is equal to 180° at perilune and to 0°, or 360°, at apolune.

Let us first focus on the orbits related to EM-L_2, namely A2, B2, and C2 (Table 1). The first one, A2 (yellow marker in Fig. 5), is the closest to the Moon, with a very low perilune radius and a minimum altitude from the Moon's surface equal to about 1525 km. Among the considered cases, it is also the unstable orbit closest to linear stability. It has been chosen as a reference for its proximity to the Moon and stability characteristics. The second orbit, B2 (orange marker), is characterised by the lowest stability in the EM-L_2 NRHO family. It is also further from the Moon and has a lower JC than A2, i.e., it has a higher energy in the EM-CR3BP. The third orbit, C2 (red marker), is a Halo orbit rather than an NRHO; however, it has been included in the analysis because it exhibits a JC value similar to that of B2, to highlight the differences in their dynamical behaviour despite comparable JCs. Furthermore, having the same energy, it is possible to imagine a low-cost transfer between the two orbits, enabling mission designers to eventually easily transfer from one to the other, depending on where it is more convenient to apply a certain disposal strategy. The three orbits can be identified by the yellow, orange, and red markers in the graphs in Fig. 5, which illustrate the evolution of the reference characteristics of the Halo family in the vicinity of EM-L_2 NRHOs. As in Fig. 3, NRHOs correspond to the orbits located between the red (unstable) and light blue (stable) areas found in the graphs on the left and in the centre.

Focusing on the orbits candidates for the analysis and related to EM-L_1, A1 (purple marker in Fig. 6) is the closest to the Moon, with a perilune radius similar to that of A2. It is characterised by a higher energy with respect to A2 (lower JC) and a lower stability. B1 (light blue marker) is chosen to have the highest JC in the EM-L_1 NRHO range. Finally, C1 (blue marker) is a Halo orbit, and it is identified by a JC similar to that of B1. The choice of this orbit has been made following the same logic as for the choice of C2. All three orbits can be found in Fig. 6, illustrating the evolution of reference characteristics along the EM-L_1 Halo family when in the vicinity of NRHOs, and are identified by a purple, light blue and blue mark, respectively. The NRHO range is defined by the red (unstable) and light blue (stable) regions, also in this case.

4. Heliocentric disposal

In this Section, the heliocentric disposal design is detailed, and the results obtained for the candidate orbits are reported.

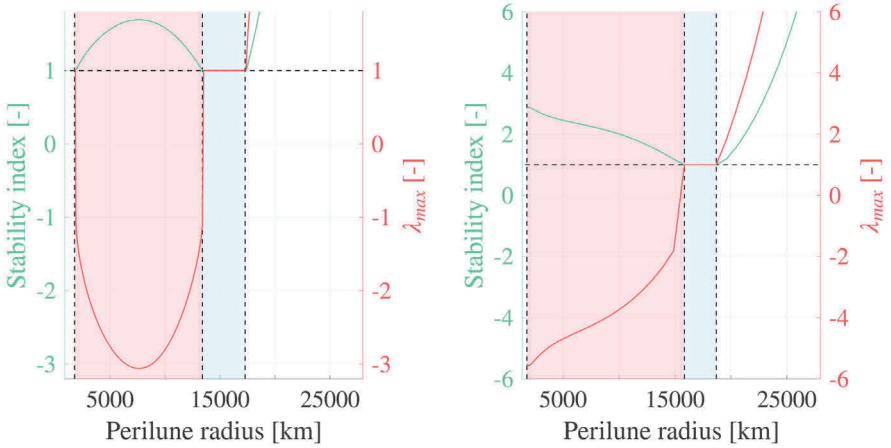

Fig. 3. Evolution of the SI (green) and of the maximum eigenvalue of the monodromy matrix, λ_{max}, (red) as a function of the perilune radius for orbits belonging to the NRHO regime in L_2 (left side of the graph) and L_1 (right side of the graph) or close by. Red regions: linearly unstable NRHOs. light blue regions: linearly stable NRHOs. (For interpretation of the references to colour in this figure legend, the reader is referred to the web version of this article.)

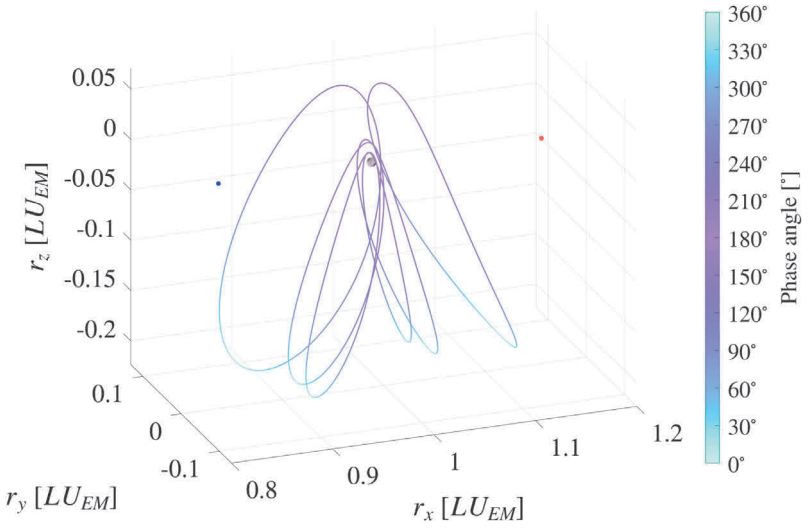

Fig. 4. Orbits considered in the analysis, represented as a function of the phase angle. EM-L_2 is marked as the red dot, EM-L_1 as the blue one. Halo orbits are the largest orbits in the graph, the closest to L_1 and L_2, respectively. (For interpretation of the references to colour in this figure legend, the reader is referred to the web version of this article.)

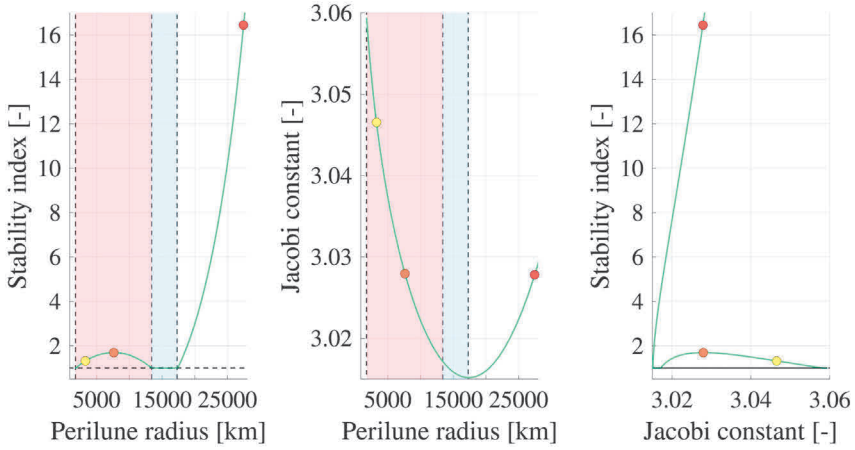

Fig. 5. Evolution of the reference characteristics of the Halo family in the vicinity of EM-L_2 NRHOs. The three orbits candidates for the analysis are identified by the yellow (A2), orange (B2), and red (C2) marks. A dashed black horizontal line identifies $SI = 1$. (For interpretation of the references to colour in this figure legend, the reader is referred to the web version of this article.)

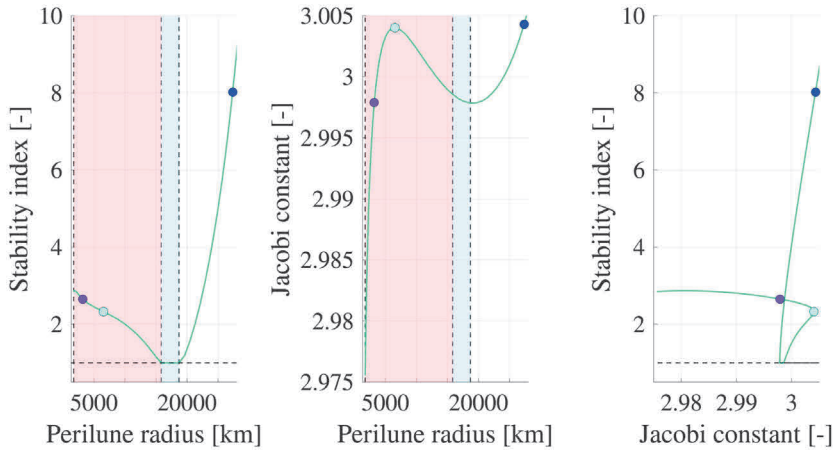

Fig. 6. Evolution of the reference characteristics of the Halo family in the vicinity of EM-L_1 NRHOs. The three orbits candidates for the analysis are identified by the purple (A1), light blue (B1), and blue (C1) marks. A dashed black horizontal line identifies $SI = 1$. (For interpretation of the references to colour in this figure legend, the reader is referred to the web version of this article.)

4.1. Heliocentric disposal design

The heliocentric disposal is designed following a two-impulse trajectory, escaping first the EM and then the SE system. Once crossed SE-L_1 or L_2, the ZVCs of the SE system are closed to prevent the spacecraft from re-entering the Earth vicinity. To insert a spacecraft on the unstable manifold of an LPO, its direction must be evaluated locally for a certain value of θ. The direction of the unstable manifold at $\theta_0(t_0) = 0°$, $\boldsymbol{\Lambda}^{\boldsymbol{u}}(\theta_0)$, corresponding to the orbit apocentre, can be computed along the direction of the eigenvector corresponding to the maximum real eigenvalue of the monodromy matrix, λ_{max}. The direction of the unstable manifold associated with other phase angles, $\boldsymbol{\Lambda}^{\boldsymbol{u}}(\theta)$, is mapped through the state transition matrix, $\boldsymbol{\Phi}(t_0, t)$, computed between t_0 and t, associated with the phase angle $\theta(t)$, where:

$$\boldsymbol{\Lambda}^{\boldsymbol{u}}(\theta) = \boldsymbol{\Phi}(t_0, t)\boldsymbol{\Lambda}^{\boldsymbol{u}}(\theta_0) \tag{18}$$

Normalising $\boldsymbol{\Lambda}^{\boldsymbol{u}}(\theta)$, $\hat{\boldsymbol{\Lambda}}^{\boldsymbol{u}}(\theta)$ is obtained, which represents the local linear approximation of the unstable manifold direction. Consequently, an initial condition of a trajectory on the unstable manifold can be computed as:

$$\boldsymbol{x}_{\boldsymbol{0}}^{\boldsymbol{u}}(\theta) = \boldsymbol{x}_{\boldsymbol{0}}(\theta) \pm \varepsilon\, \hat{\boldsymbol{\Lambda}}^{\boldsymbol{u}}(\theta) \tag{19}$$

where $\boldsymbol{x}_{\boldsymbol{0}}(\theta)$ is the state of the LPO corresponding to a certain value of θ, and ε is a perturbation considerable enough to allow for the object to depart from the reference LPO, but also small enough to not violate linearity. This value can generally range between 10^{-6} and 10^{-4} for the EM system and, in this work, is fixed equal to 10^{-4}. The presence of ε can be physically interpreted either as an initial ΔV, of an order of magnitude of $10^{-2} - 10^{-3}$ m/s, or equivalently as an infinitesimal perturbation applied to the nominal state of the periodic orbit. It is important to remark that the manifold parametrisation depends on ε, i.e., a variation in ε produces a corresponding shift in the phase angle θ. Moreover, the chosen value of ε influences the escape timescales: a larger ε generally corresponds to a faster escape.

The direction along which this initial ΔV (or perturbation) is given can be chosen to be either positive or negative, as shown in Eq. (19). For the present study, the value of ε was chosen to be always arbitrarily positive for NRHOs, i.e., when $\lambda_{\max} < 0$, and with the sign leading to select the branch directed towards EM-L_2 for Halo orbits. Once the spacecraft is injected into the unstable manifold, it follows its natural dynamics and may:

1. exit the EM-L_2 bottleneck,
2. impact the Moon, or
3. remain bounded within the EM system for the entire simulation time (12 months).

In the latter two cases, the simulation is stopped, and the corresponding conditions are recorded. If the trajectory exits EM-L_2, propagation continues in the SE-CR3BP, switching the dynamical model once the Sun's gravitational influence exceeds that of the Moon. The spacecraft then keeps following the unstable manifold dynamics. In the SE system, similar outcomes to the previous simulations can be obtained: exit from the SE region, either from L_1 or L_2, lunar impact, Earth impact, or failure to escape within 12 months. Note that there is always the possibility of switching back to the EM-CR3BP if lunar gravity becomes dominant again.

For the trajectories that escape the Earth vicinity through either SE-L_1 or L_2, the SE ZVCs are closed by means of a manoeuvre that prevents the spacecraft from returning to the Earth neighbourhood, as long as the SE-CR3BP approximation holds. This manoeuvre is designed using an energetic approach: it is applied in the anti-tangential direction of the spacecraft velocity at a selected location and decreases the spacecraft's energy sufficiently to virtually close the SE ZVCs at the L_1 or L_2 bottleneck, depending on where the escape happened. To achieve this, it is sufficient to impose $JC''_{SE} \geq JC_{SE-L_i}$, where JC''_{SE} is the JC of the trajectory computed at the point where the manoeuvre is applied, and JC_{SE-L_i} is the JC associated with either SE-L_1 or SE-L_2. The ΔV required to close the ZVCs can thus be computed as:

$$\Delta V = -\|\boldsymbol{v}'\| \pm \sqrt{\|\boldsymbol{v}'\|^2 - \Delta JC} \tag{20}$$

where $\boldsymbol{v}'$ is the spacecraft velocity in the SE-CR3BP before the ZVC-closure manoeuvre, and $\Delta JC = JC_{L_i} - JC'$, i.e., the difference between the JC at the targeted Lagrange point and that of the trajectory before closure. The solution corresponding to the minus sign in the second term of Eq. (20) is not considered in the analysis, as it results in a larger closure ΔV compared to the solution obtained with the plus sign. Note that, in this work, the direction of the ZVCs closure manoeuvre is fixed to be tangential to the spacecraft velocity to reduce the dimensionality of the solution space, but an extended analysis including additional possible manoeuvre directions could be explored in future work.

As a final remark, in this work, heliocentric disposal is considered achieved whenever a trajectory exits the Earth vicinity through either SE-L_1 or SE-L_2 and the ZVCs closure manoeuvre is applied. This guarantees that the CR3BP approximation remains valid. However, at least two further points must be highlighted:

1. From a long-term sustainability point of view, escaping through SE-L_2 may be preferable to escaping through SE-L_1, to avoid

having uncontrolled objects orbiting the interior region of the solar system. Although both options are treated as viable in this analysis, they are distinguished in the subsequent discussion to allow for a focus on a preferred option if needed.

2. The results obtained here are valid only as far as the approximations previously discussed hold. Manifold dynamics map the evolution of escape trajectories in a high-fidelity, ephemeris-based dynamical model, but a final disposal design must be supported by long-term simulations performed also in these more complete models.

4.2. Simulation and results

In this Section, the results related to heliocentric disposal for the six orbits listed in Section 3 are presented. The reference LPOs are identified only by their labels; for a detailed description of their characteristics, see Table 1.

The analysis begins with the three LPOs associated with L_2, namely A2, B2, and C2. In Fig. 7, the trajectories along the unstable manifold of orbit A2 are shown, propagated either until escape or for the full 12 months integration interval whenever escape or impact does not occur. Results are presented as a function of the phase angle of the departure point, θ_0, discretised with a resolution of 2°, and for four different values of α_0, the phase between the SE and EM systems at departure from the LPO, set as 0°, 90°, 180°, and 270°.

What is of particular interest is both the shape and the evolution of the escape trajectories, as well as the strong influence exerted by the phase angles θ_0 and α_0. A symmetry in the solution space with respect to α_0 can be hypothesised by examining the four values for which the escape trajectories are shown. It is also interesting to observe that trajectories departing from a given point on the LPO, characterised by a specific value of θ_0, tend to escape through L_2 for a certain value of α_0, and through L_1 for the same value of α_0 plus 180°. This behaviour is of significant interest, as it may indicate an intertwined symmetry in the way these two parameters influence the simulation outcomes. In Fig. 8, the cost of the ZVCs closure manoeuvre is reported for the four considered cases as a function of both θ_0 and the time spent by the spacecraft on the manifold before performing the ZVCs closure manoeuvre.

The graph is coloured in yellow when the unstable manifold trajectories escape the EM system but do not cross either SE-L_1 or SE-L_2 within the considered time frame; in purple for lunar impacts and in red for Earth impacts. Whenever escapes are present, they are overlaid by either a white or a blue region: the white area corresponds to escape through SE-L_2, while the blue area corresponds to escape through SE-L_1. Symmetry on the results obtained between a certain α_0 and $\alpha_0+180°$ is evident also in this second representation of the results. The solution space appears scattered, a behaviour attributable to the strong linear stability of the initial NRHO and to its proximity to the Moon, both of which interfere with the escape. On the left-hand side of the plot, the graph remains empty even for cases that eventually succeed: for low ToF values, disposal is not feasible because neither SE-L_2 nor L_1 has yet been crossed. Once the crossing occurs, the disposal cost is initially very high and then gradually decreases as the ToF increases. This trend is consistent with the behaviour reported in [22] for no-return escape trajectories departing from EM-L_2, studied considering only the EM-CR3BP.

The ΔVs required to close the ZVCs are generally quite large, even if, when allowing for long ToFs, the disposal cost can reach values in the order of 25–50 m/s. To aid the visualisation of this aspect, markers have been added to the graphs shown in figures such as Fig. 8. These markers indicate, as θ_0 varies, the minimum ToF required to reach conditions under which the total ΔV is equal to 50 m/s. The long ToFs observed are a reasonable result, as A2 lies very close to the Moon and is therefore inherently disadvantaged compared to other orbits when attempting to escape the SE system, leading to longer ToFs. The corresponding JC gap to be covered by the ZVCs closure manoeuvre is significant, leading to a substantial ΔV requirement when the SE-CR3BP dynamic only is considered. Also, as was observed in [22] for the EM system only, once the trajectory exits the ZVCs of the reference system, the ZVCs closure manoeuvre ΔV diminishes as the distance from the dominant body in the system increases, i.e., the minimum ΔV is reached at the apocentre of the disposal trajectory with respect to the Sun. What differs with respect to the EM-only analysis is the timescale required to achieve escape. In the present case, the escape time is naturally more extended, and as a consequence, the apocentre condition is not always reached within the considered time frame, even if the relationship between the ΔV and the distance from the Sun remains clear.

The evolution of the escape trajectories is not reported here for the other LPOs at L_2, as it closely resembles the behaviour observed for A2. The corresponding evolution of the ΔV for orbit B2 is instead shown in Fig. 9.

The symmetry of the solutions with respect to α_0 is clearly visible also in Fig. 9, when the orbit B2 is considered. In this case, the evolution of the escape behaviour is considerably less scattered than what was observed for orbit A2. This is consistent with the fact that B2 is characterised by a lower linear stability (the lowest within the NRHO family) and by a larger distance from the Moon. The disposal ΔV costs and time scales are similar to what was observed for A2. The results obtained for orbit C2 are reported in Fig. 10.

The results obtained for C2 are very similar to those obtained for B2 (recall that the two orbits share the same JC, although C2 is a Halo orbit rather than an NRHO). It is also interesting to observe that the shape of the ΔV evolution for B2 with $\alpha_0 = 90°$ appears to resemble that of C2 with $\alpha_0 = 0°$. The same holds for other pairs of α_0 values. Moreover, in this case, the lower linear stability with respect to B2 does not seem to have a strong influence on the results.

Let us now proceed to analyse the dynamics of the escape trajectories for A1, shown in Fig. 11.

The trajectory evolution is similar to what was observed for A2 in Fig. 7, even though A1 is an orbit centred around EM-L_1. The evolution of the ΔV for A1 is reported in Fig. 12.

The colours in the graph correspond to the same cases described previously. An additional outcome is included: the possibility that no escape from the EM system occurs throughout the entire integration interval. Whenever this happens, the plot remains white for the overall range of ToFs considered. The same general conclusions drawn for the L_2 orbits remain valid. Compared with A2, which has approximately the same distance from the Moon as A1, escape appears to occur over a broader interval of θ_0 (for a given value of α_0). This suggests that, in this case, the manifold may be governed by a less chaotic dynamical behaviour, an aspect that could be attributed to the lower linear stability of A1 with respect to A2. The symmetry with respect to α_0 is clearly visible in this case as well, and the same behaviour is observed for B1 and C1. The evolution of the ZVCs closure ΔV for B1 is reported in Fig. 13.

The behaviour observed is consistent with that of the other orbits analysed. An interesting aspect in this case is that, despite the presence of manifold trajectories that do not escape the EM system at all, the escape behaviour in the SE system is well structured and concentrated around specific values of θ_0, similarly to what was observed for A1.

Finally, the results obtained for C1 are presented in Fig. 14.

In this case, the evolution of the escape behaviour is highly chaotic, almost as much as what was observed for A2. A plausible explanation is that, for C1, the increased distance from the Moon, which corresponds, in this case, also to an increased distance from L_2, leads to a manifold structure that is unstable and strongly nonlinear, making it poorly suited for heliocentric disposal. It is also worth noting that orbits B1 (NRHO) and C1 (Halo orbit) share the same JC, just as B2 and C2 do. For B1 and C1, it is reasonable to hypothesise that, having comparable energy levels, low-cost transfers between the two orbits may exist through heteroclinic connections between their stable and

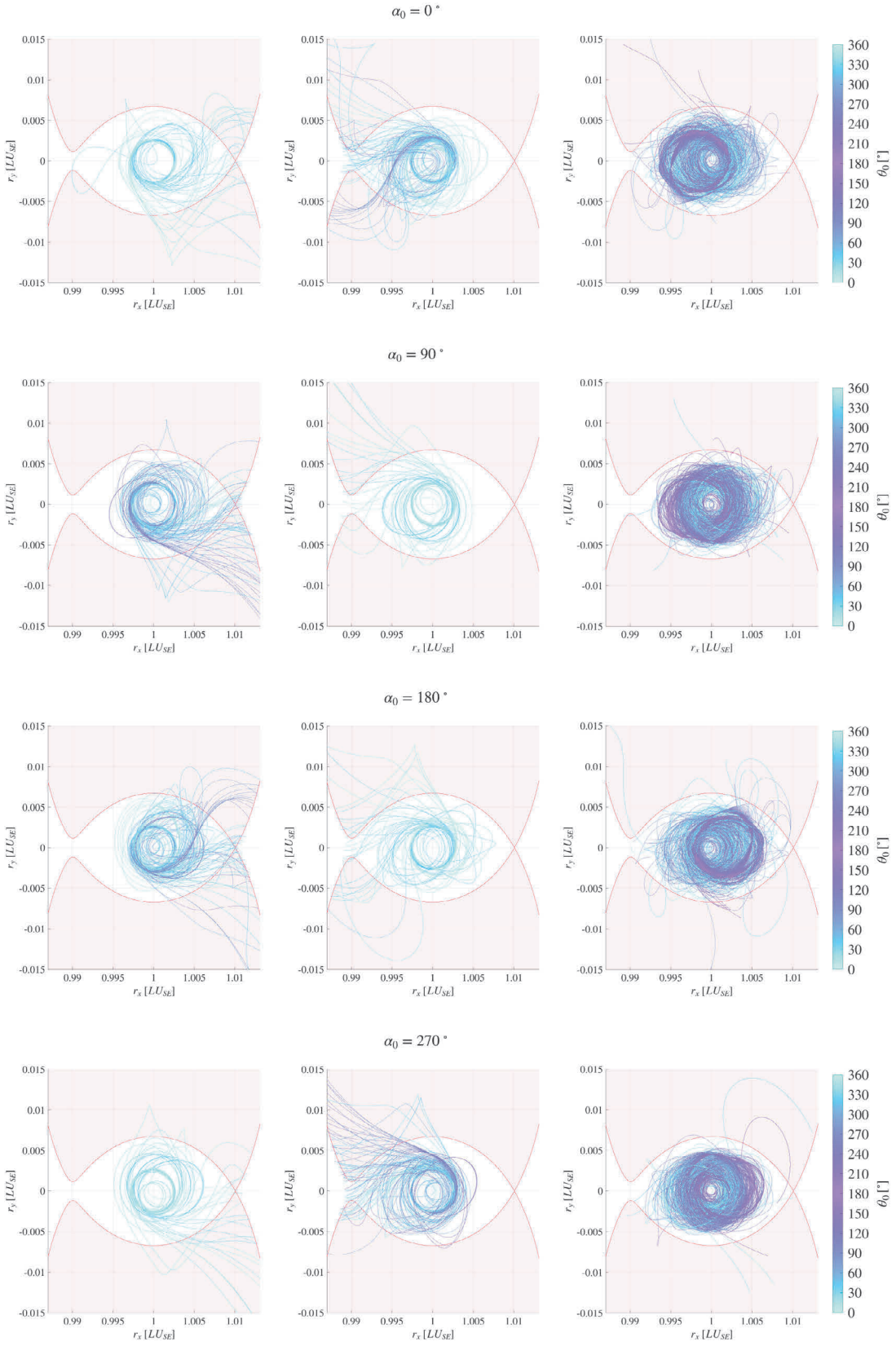

Fig. 7. Unstable manifold trajectory evolution in the SE system as a function of the phase angle θ_0, shown for four different values of α_0 (label on top of each graph). From left to right in each panel: escape through SE-L_2, escape through SE-L_1, non-escaping and non-impacting trajectories — Orbit A2.

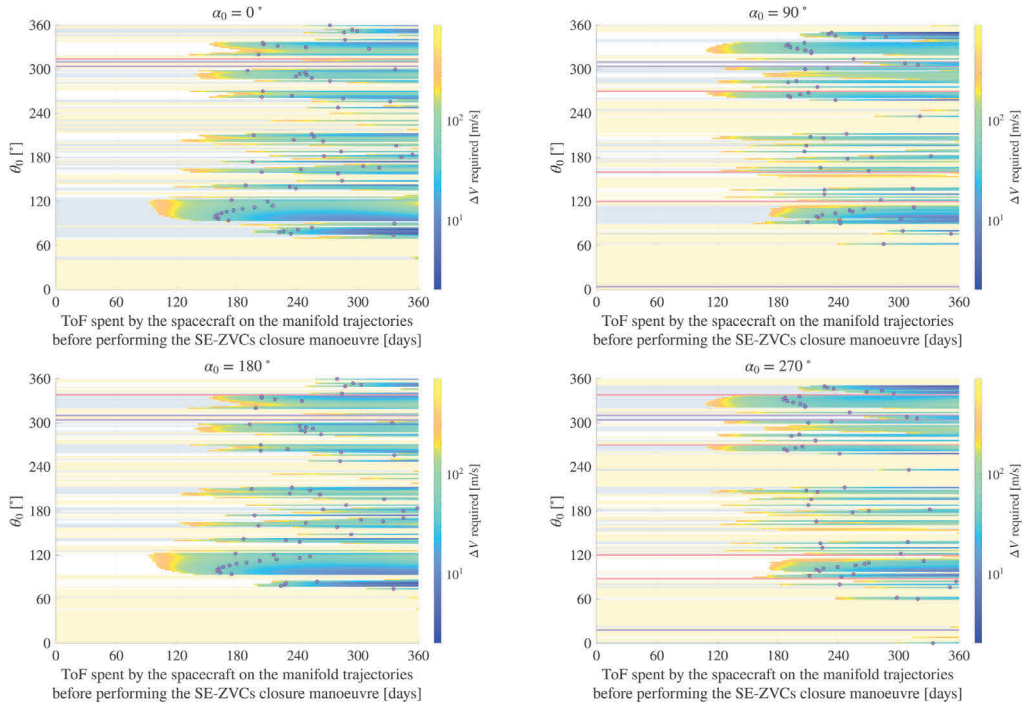

Fig. 8. Orbit A2 — Heliocentric disposal cost as a function of the phase angle θ_0 and of the ToF spent on the manifold before performing the ZVC-closure manoeuvre, shown for four different values of α_0. Purple regions indicate lunar impacts, red regions indicate Earth impacts, and yellow regions correspond to no escape. The blue escape region denotes escape through SE-L_1, while the white escape region denotes escape through SE-L_1. Markers indicate the earliest times at which a total disposal ΔV of 50 m/s is achieved. The ΔV evolution is reported in logarithmic scale. (For interpretation of the references to colour in this figure legend, the reader is referred to the web version of this article.)

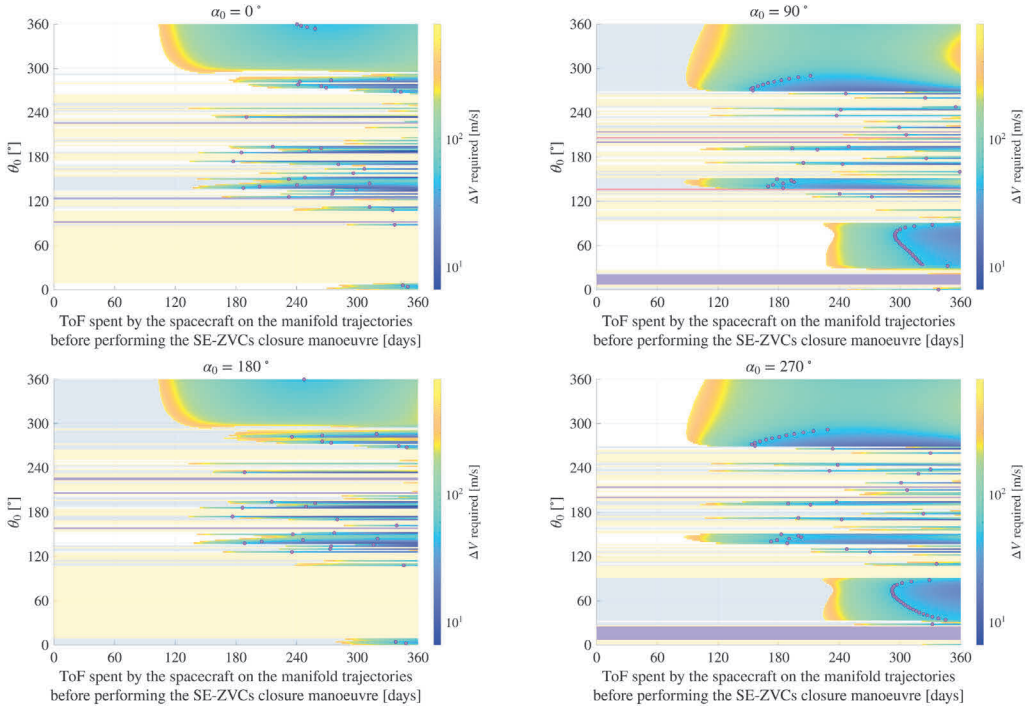

Fig. 9. Orbit B2 — Heliocentric disposal cost as a function of the phase angle θ_0 and of the ToF spent on the manifold before performing the ZVC-closure manoeuvre, shown for four different values of α_0. Purple regions indicate lunar impacts, red regions indicate Earth impacts, and yellow regions correspond to no escape. The blue escape region denotes escape through SE-L_1, while the white escape region denotes escape through SE-L_1. Markers indicate the earliest times at which a total disposal ΔV of 50 m/s is achieved. (For interpretation of the references to colour in this figure legend, the reader is referred to the web version of this article.)

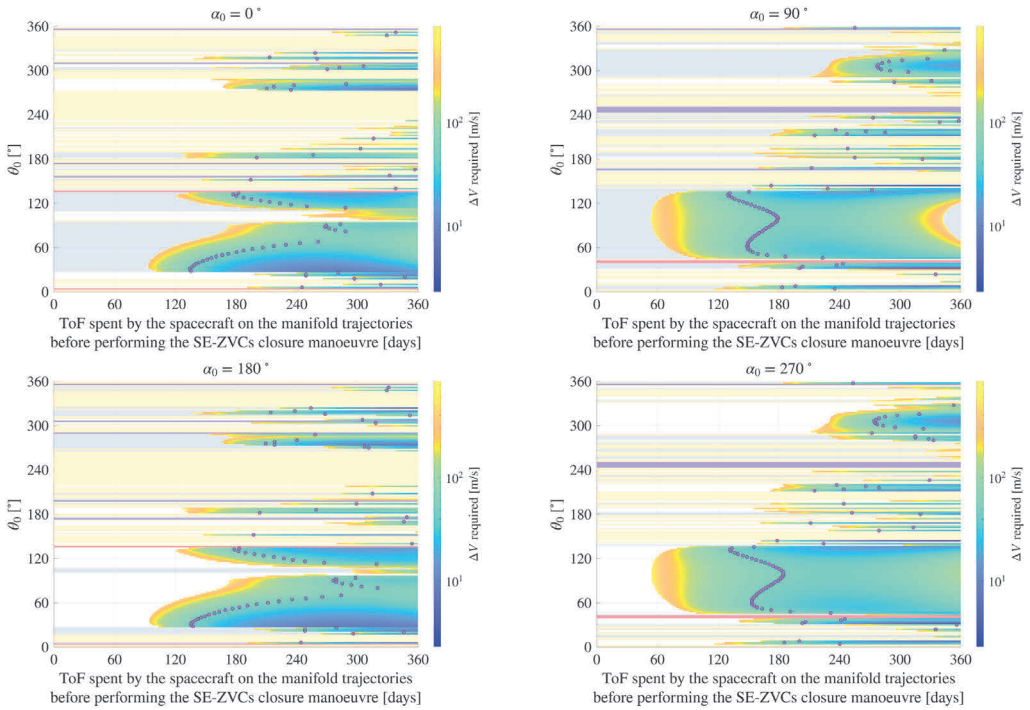

Fig. 10. Orbit C2 — Heliocentric disposal cost as a function of the phase angle θ_0 and of the ToF spent on the manifold before performing the ZVC-closure manoeuvre, shown for four different values of α_0. Purple regions indicate lunar impacts, red regions indicate Earth impacts, and yellow regions correspond to no escape. The blue escape region denotes escape through SE-L_1, while the white escape region denotes escape through SE-L_1. Markers indicate the earliest times at which a total disposal ΔV of 50 m/s is achieved. The ΔV evolution is reported in logarithmic scale. (For interpretation of the references to colour in this figure legend, the reader is referred to the web version of this article.)

unstable manifolds [23]. Such connections could allow a spacecraft to be transferred from its original operational orbit (for example, C1) to a secondary orbit (for example, B1) from which heliocentric disposal is more favourable, for then performing the disposal manoeuvre. To summarise, this work has shown that low-cost heliocentric disposal solutions can be achieved for the considered orbits by appropriately selecting the initial perturbation ε (or initial ΔV) used to insert the spacecraft onto the unstable manifold, and by targeting specific values of θ_0 and α_0. One of the main limitations of this approach is the long ToF required to achieve escape, particularly when a ZVC closure manoeuvre is considered, which may pose operational difficulties. It is worth noting, however, that the ToF to escape strongly depends on the initial perturbation ε: as reported, for example, in [9], increasing the initial ΔV generally leads to shorter ToFs, although this implies not considering the linear approximation for the unstable manifold adopted in this work. Finally, the necessity of the ZVCs closure manoeuvre in ephemeris-based dynamics remains an open question. These points will be addressed in future work.

5. Controlled lunar impact

In this Section, the controlled lunar impact disposal design is detailed, and the results obtained for the candidate orbits are reported.

5.1. Controlled lunar impact disposal design

Controlled lunar impact disposal trajectories are modelled as three-impulse transfers, obtained by solving a multiple-shooting Sequential Quadratic Programming (SQP) problem. The objective function minimises the total disposal ΔV, while enforcing the constraint that the trajectory must impact the lunar surface. As a first step, disposal options are searched within the EM-CR3BP dynamical framework. The first impulse is applied, analogously to the heliocentric disposal strategy, to insert the spacecraft onto the unstable manifold of the selected operational periodic orbit. The derivation and definition of the unstable manifolds follow the same general principles discussed for the heliocentric disposal case. The sign of the perturbation ε is again fixed to be positive for NRHOs. For Halo orbits, instead, the sign is chosen such that the selected branch of the unstable manifold is the one directed towards the Moon. Consequently, as in the heliocentric disposal case, both the magnitude and direction of the first ΔV are fixed a priori. Once the spacecraft is inserted onto the unstable manifold, it naturally tends to approach the Moon for at least some of the considered phase angle values. The multiple-shooting algorithm then applies relatively small corrections to the trajectory in terms of ΔV to guarantee a lunar impact by lowering the trajectory perilune.

It is important to emphasise that the adopted optimisation strategy leads to a local optimum of the solution space rather than a global one. As a consequence, the solutions obtained are optimal only within the neighbourhood of trajectories consistent with how the problem was initially formulated. To more globally assess the impact of, for instance, the number of manoeuvres on the results, a broader analysis should be performed in which the number of impulses is explicitly included as a design variable. This aspect is important to highlight because, in principle, even a single impulsive manoeuvre, when combined with the initial insertion onto the unstable manifold, could be sufficient to achieve a lunar impact, if longer ToFs are considered acceptable [24]. However, multiple-shooting schemes generally converge more reliably when an adequate initial guess is provided; for this reason, and considering that additional constraints must be included in the simulation, the three-impulse strategy is preferred. Also, to limit the number of optimisation variables, the direction of each manoeuvre is fixed to be tangential to the spacecraft velocity, although its sign may be either positive or negative. The considerations on how this modelling choice restricts or reshapes the design space could be further investigated in future works as well.

As in classical optimisation problems, the objective function is defined to minimise the total ΔV. A lunar-impact condition is imposed as a

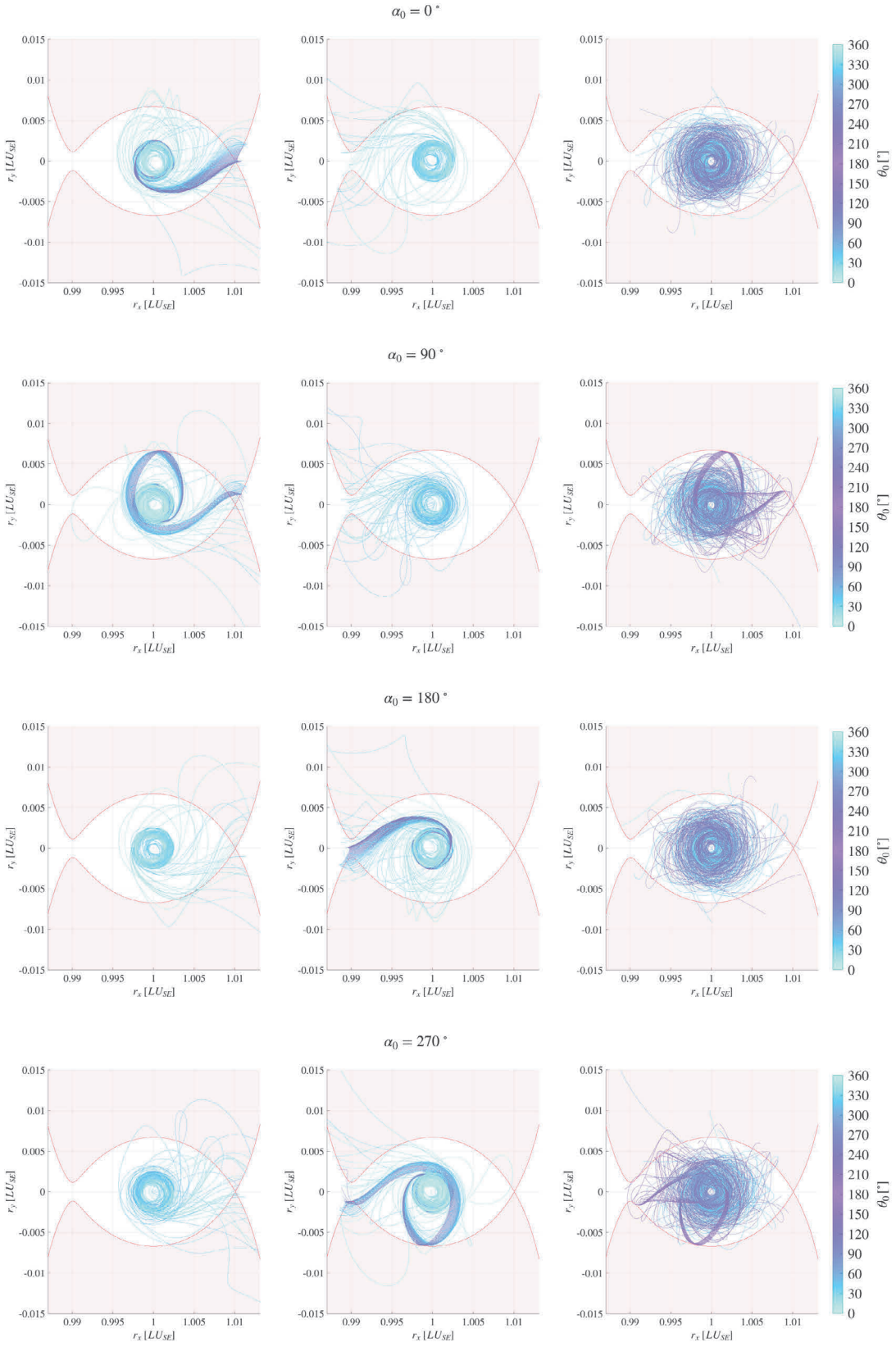

Fig. 11. Unstable manifold trajectory evolution in the SE system as a function of the phase angle θ_0, shown for four different values of α_0. From left to right in each panel: escape through SE-L_2, escape through SE-L_1, non-escaping and non-impacting trajectories — Orbit A1.

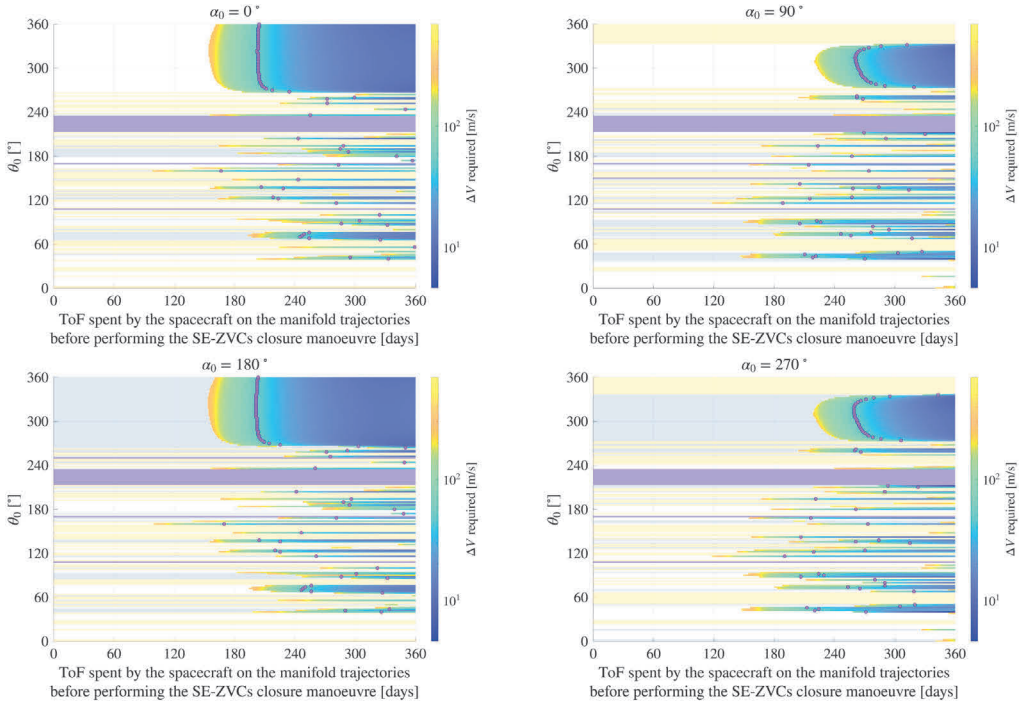

Fig. 12. Orbit A1 — Heliocentric disposal cost as a function of the phase angle θ_0 and of the ToF spent on the manifold before performing the ZVC-closure manoeuvre, shown for four different values of α_0. Purple regions indicate lunar impacts, red regions indicate Earth impacts, and yellow regions correspond to no escape. The blue escape region denotes escape through SE-L_1, while the white escape region denotes escape through SE-L_1. Markers indicate the earliest times at which a total disposal ΔV of 50 m/s is achieved. The ΔV evolution is reported in logarithmic scale. (For interpretation of the references to colour in this figure legend, the reader is referred to the web version of this article.)

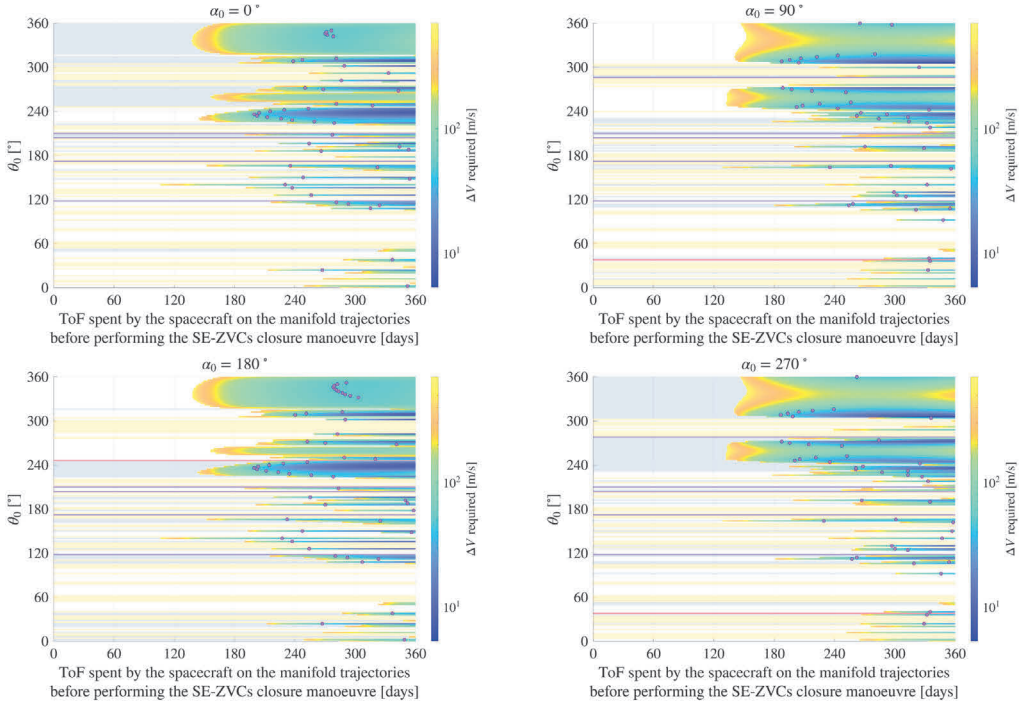

Fig. 13. Orbit B1 — Heliocentric disposal cost as a function of the phase angle θ_0 and of the ToF spent on the manifold before performing the ZVC-closure manoeuvre, shown for four different values of α_0. Purple regions indicate lunar impacts, red regions indicate Earth impacts, and yellow regions correspond to no escape. The blue escape region denotes escape through SE-L_1, while the white escape region denotes escape through SE-L_1. Markers indicate the earliest times at which a total disposal ΔV of 50 m/s is achieved. The ΔV evolution is reported in logarithmic scale. (For interpretation of the references to colour in this figure legend, the reader is referred to the web version of this article.)

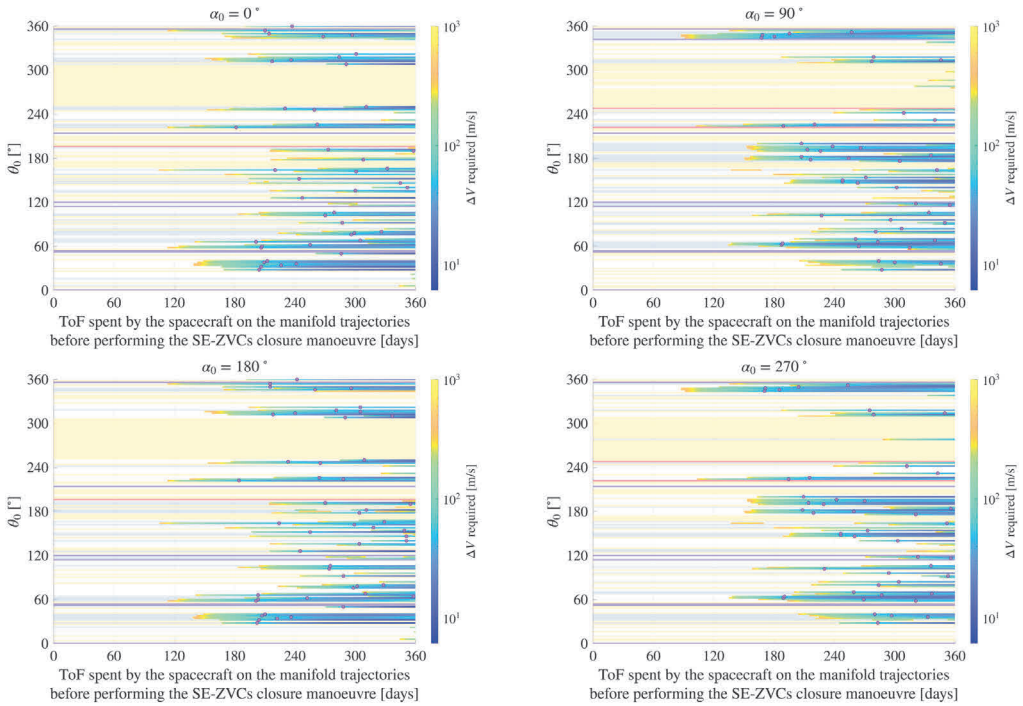

Fig. 14. Orbit C1 — Heliocentric disposal cost as a function of the phase angle θ_0 and of the ToF spent on the manifold before performing the ZVC-closure manoeuvre, shown for four different values of α_0. Purple regions indicate lunar impacts, red regions indicate Earth impacts, and yellow regions correspond to no escape. The blue escape region denotes escape through SE-L_1, while the white escape region denotes escape through SE-L_1. Markers indicate the earliest times at which a total disposal ΔV of 50 m/s is achieved. The ΔV evolution is reported in logarithmic scale. (For interpretation of the references to colour in this figure legend, the reader is referred to the web version of this article.)

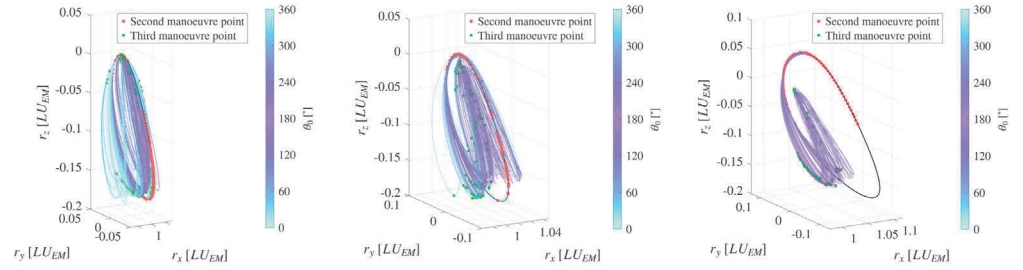

Fig. 15. Controlled lunar impact disposal trajectories evolution as a function of the phase angle θ_0 for the three LPOs in L_2 selected as candidates for the analysis. From left to right in the graph, disposal trajectories leaving from A2, B2 and C2.

constraint, together with a maximum allowable ToF of 20 days, i.e., the time the spacecraft is allowed to remain on the disposal trajectory before impacting the lunar surface. This constraint is introduced because the region in which the spacecraft orbits is influenced not only by the EM-CR3BP dynamics, but also significantly by the Sun's gravity and by lunar gravitational harmonics. Therefore, imposing a limit on the ToF ensures that the actual dynamics can be reasonably approximated by the CR3BP over the considered interval, maintaining a reasonable accuracy in the results obtained. Moreover, constraints are included in the optimisation to prevent impacts on protected regions as well. The Moon is not only of significant scientific interest, but it also contains historical and cultural heritage sites that must be preserved, as well as areas of particular relevance for future applications, which cannot reasonably be used as disposal sites. Current guidelines regarding these aspects do not always fully agree; however, for the present study, two main constraints have been considered:

- *Avoidance of historical sites.* Recommendations provided in [25] strongly advise avoiding impacts within a radius of at least 2 km from locations identified as historically significant, such as the Apollo landing sites. It is also suggested that these sites be overflown only on trajectories tangent to the lunar surface, to avoid passing over them during the descent phase. This latter aspect has not been included in the present work but should be considered in future studies, for instance by excluding impact trajectories with longitudes similar to the ones of protected sites but at higher latitudes. Such a constraint would prevent contamination from material released by the spacecraft during descent. In this study, historical landing sites from the Apollo, Luna, Surveyor, Chang'e, GRAIL, and LADEE missions are considered. The coordinates of these sites are retrieved from the Lunar Reconnaissance Orbiter Camera (LROC) database [25,26].
- *Avoidance of areas of particular scientific interest.* The Committee on Space Research (COSPAR) specifies that planetary-protection guidelines must be enforced for landings within Permanently Shadowed Regions (PSRs) or near the lunar poles, i.e., at latitudes higher than 86°N or lower than 79°S [27]. Although landings in these areas are possible, they are not suitable candidates for disposal operations, as enforcing planetary-protection requirements during an uncontrolled or semi-controlled disposal descent phase

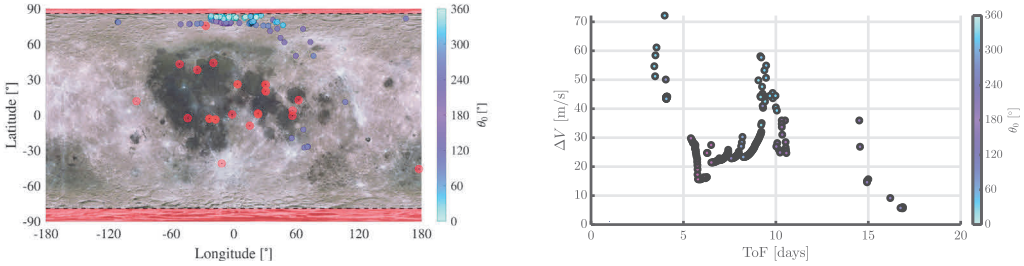

Fig. 16. Left: impact locations on the Moon surface as a function of the departure phase angle θ_0. Right: evolution of the disposal ΔV as a function of the ToF and the departure phase angle θ_0 - Orbit A2. (For interpretation of the references to colour in this figure legend, the reader is referred to the web version of this article.)

is considerably more difficult. Moreover, given their scientific importance, PSRs and polar regions should not be used as disposal sites. A latitude constraint is introduced in the optimisation process to avoid impacts near the lunar poles. No explicit constraint has been included for PSRs; however, since most PSRs are located close to the poles, they are implicitly avoided by the latitude bound. Future work should incorporate a comprehensive catalogue of PSRs into the simulations, following a similar approach to that adopted for historical heritage sites.

It is important to note that, since no universally accepted guidelines currently exist, additional regions could in principle be considered protected as well. Nevertheless, the areas included in this study are those identified as the most relevant from both scientific and cultural perspectives, and they are also the ones most consistently recognised across multiple reference documents. As a final comment, it may also be reasonable to consider, in future studies, introducing constraints on allowed impact regions rather than on forbidden ones, directing all disposed spacecraft towards well-defined, graveyard-like locations on the lunar surface. However, because current regulations do not adopt such an approach, the present work instead focuses on avoiding regions of interest. Impact areas constraints are imposed as nonlinear optimisation constraints on longitude and latitude. These two parameters are computed using the impact locations expressed in the Mean Earth/Polar Axis (ME) Moon-centred lunar body-fixed reference frame, which is the recommended system for lunar cartographic applications [28]. The rotation matrix between the Moon-centred J2000 inertial and the ME Moon-centred reference frame is provided by SPICE, thanks to the *cspice_pxform* routine. The departure date from the LPO for all impact trajectories is fixed as April 15th 2026.

5.2. Simulations and results

In the following Section, the results obtained for the controlled lunar-impact disposal design are presented. First, solutions obtained within the EM-CR3BP are shown for all six reference orbits; subsequently, a selection of impact trajectories is refined using an ephemeris-based dynamical model for A2 and A1. Within the CR3BP framework, solutions are reported as functions of the phase angle θ_0, discretised with a resolution of 2°, yielding a total of 181 distinct initial conditions along the orbit from which the spacecraft departs. In Fig. 15, lunar impact trajectories for A2, B2 and C2 are reported.

It is evident from the evolution of the lunar impact trajectories that the farther the reference orbit lies from the Moon, the more challenging it becomes to achieve disposal through controlled impact. For A2 (leftmost graph of Fig. 15), disposal through lunar impact is obtained for all the considered initial conditions. The second manoeuvre point almost always lies very close to the periodic orbit itself, indicating that the time spent by the spacecraft on the unstable manifold before performing any manoeuvre is nearly zero for the majority of conditions and that, in practise, two $\Delta V s$, including the initial perturbation along the manifold, may be sufficient to impact the Moon successfully. The third manoeuvre is performed close to the apolune for the majority of the solutions, which is consistent with the theoretical expectation that applying an impulse near apolune is the most effective way to lower the perilune, driving the spacecraft towards impact. This behaviour suggests that the initial unstable manifold trajectories naturally pass very close to the Moon.

For B2, the evolution of the disposal trajectories is less regular as θ_0 varies, leading to multiple overlapping patterns. The second manoeuvre point once again tends to lie close to the unstable manifold insertion point or near the NRHO itself, especially around perilune. The third manoeuvre is still performed near apolune for most solutions, although in some cases the corrective impulse that ensures impact occurs closer to the Moon. While most unstable manifold trajectories for B2 can be successfully refined into impact trajectories, for C2 this is true only for a limited subset of θ_0 values near perilune. This is due to the fact that, for Halo orbits, the unstable manifold generally passes farther from the Moon than in the NRHO case, making controlled impact more difficult to impose. The locations of the second and third manoeuvre points for C2 remain consistent with the behaviours observed for A2 and B2. In this case, if controlled lunar-impact disposal were required for a spacecraft operating on C2, it could be advantageous to exploit heteroclinic connections to first transfer the spacecraft to B2 and then perform the disposal from there, where the geometry is more favourable.

In Fig. 16, the impact locations on the Moon surface and the evolution of the total ΔV as a function of the ToF and the departure phase angle θ_0 are shown for orbit A2.

Impact locations are reported as a function of latitude and longitude on the lunar surface, computed in the ME reference frame. The red regions at the top and bottom of the plot correspond to latitudes excluded by the constraint adopted to avoid impacts near the lunar poles. Red dots indicate historical sites that must not be impacted. Note that the actual protected regions are indicated by the black point at the centre of each red area; these regions appear larger in the plot just to help with the visualisation. All protected locations are successfully avoided. Impact points tend to cluster in specific areas as a function of θ_0, with most of them located near the lunar North pole. This is expected, since for A2 the disposal trajectories closely resemble the associated unstable manifold trajectories; thus, impact is achieved simply by lowering the perilune, which for most of the trajectories of this manifold naturally lies near the lunar North pole. In the corresponding plot of ΔV as a function of the ToF and the phase angle, different solution regimes can clearly be distinguished as θ_0 varies, forming distinct Pareto-like structures. In general, lunar impact is achieved more rapidly for departures near perilune ($\theta_0 = 180°$), whereas departures near apolune ($\theta_0 = 0°, 360°$) tend to require longer ToFs if high $\Delta V s$ are to be avoided. The mean disposal cost is about 25 m/s, for a mean ToF of about 8 days.

The same results are shown in Figs. 17 and 18 for B2 and C2, respectively.

For the impact points associated with B2, the same general considerations made for A2 still hold. It should be noted that a few impact

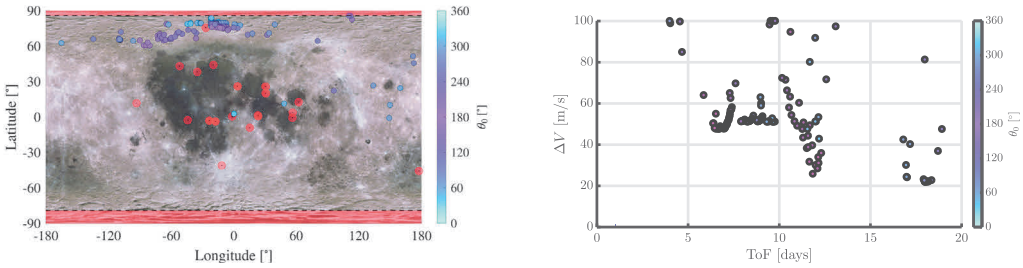

Fig. 17. Left: impact locations on the Moon surface as a function of the departure phase angle θ_0. Right: evolution of the disposal ΔV as a function of the ToF and the departure phase angle θ_0 - Orbit B2. (For interpretation of the references to colour in this figure legend, the reader is referred to the web version of this article.)

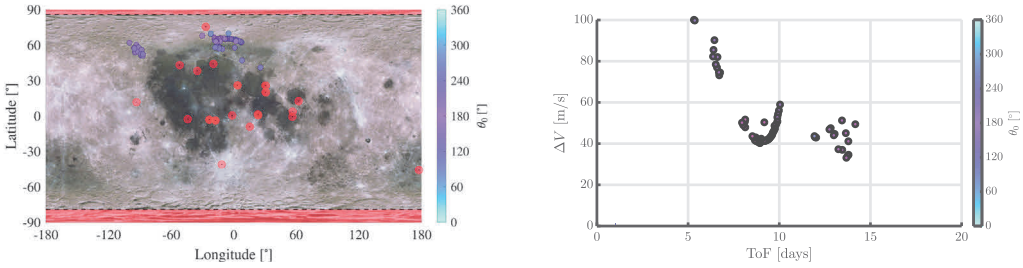

Fig. 18. Left: impact locations on the Moon surface as a function of the departure phase angle θ_0. Right: evolution of the disposal ΔV as a function of the ToF and the departure phase angle θ_0 - Orbit C2. (For interpretation of the references to colour in this figure legend, the reader is referred to the web version of this article.)

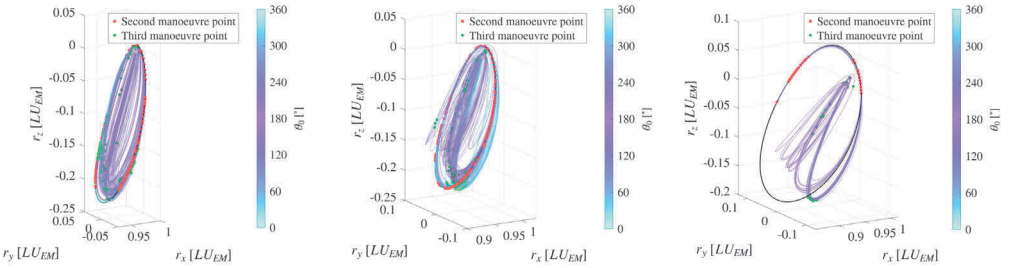

Fig. 19. Controlled lunar impact disposal trajectories evolution as a function of the phase angle θ_0 for the three LPOs in L_1 selected as candidates for the analysis. From left to right in the graph, disposal trajectories leaving from A1, B1 and C1.

points lie close to historical sites, although they remain technically outside the protected 2 km radius region surrounding them. The range of longitudes reached in this case is significantly more scattered than for A2. This behaviour is driven by the greater diversity in the dynamical behaviours exhibited by the trajectories, as well as by the larger range of ToF values leading to lunar impact in the B2 case, as also shown in the right-hand graph. In this case, departures near perilune appear to be the most favourable options, producing a region with many solutions featuring low ToF values (around 12 days) and low ΔV (approximately 30 m/s). Some trajectories require considerably higher ΔV, but the mean value remains reasonable for a disposal scenario, with the majority of solutions exhibiting a ΔV of roughly 50 m/s for a ToF of about 7 days.

For C2, only a limited subset of trajectories actually leads to successful disposal, as also highlighted in Fig. 15. Nonetheless, the trajectories that do result in impact yield promising outcomes, with impact locations clustering within two well-defined longitude ranges and a clear Pareto-like front in the ΔV versus ToF diagram. The mean ΔV remains around 45 m/s for a ToF of approximately 9 days. Disposal through controlled lunar impact remains a viable option also for C2, provided that the departure occurs for well-defined values of θ_0. Finally, for both B2 and C2, all impact points lie at high lunar latitudes, for the same reasons discussed previously for A2.

In Fig. 19, controlled lunar impact trajectories are shown for the LPO candidates for the analysis centred at L_1, going from left to right: A1, B1, C1.

The evolution of the disposal trajectories from A1 to C1 is very similar to what was observed for the L_2 LPOs, confirming that the dominant factor governing the trajectory behaviour is, in this case, the distance from the Moon. As for L_2 LPOs, the number of trajectories successfully impacting the Moon decreases for C1, and the departure phase angles leading to a successful disposal are almost entirely concentrated around the perilune region. Note that, for A1, the third manoeuvre locations are not all clearly clustered near apolune, unlike what is observed for the other orbits considered. This behaviour can be justified by the fact that, as indicated by the purple band between $\theta = 120°$ and 180° in Fig. 12, some of the unstable manifold trajectories departing from A1 naturally lead to a lunar impact even when only the manifold insertion impulse is applied, with no additional manoeuvres. This is further confirmed by the ΔV evolution shown in the right-hand plot of Fig. 20, where very low values of ΔV appear to be enough to dispose of the spacecraft for departure points with θ_0 close to the 120°–180° region.

Disposal conditions far from these lead to higher ΔVs and lower ToFs such that two very distinct regions of both ΔV and ToFs evolution and impact points can be identified in both graphs of Fig. 20, the first

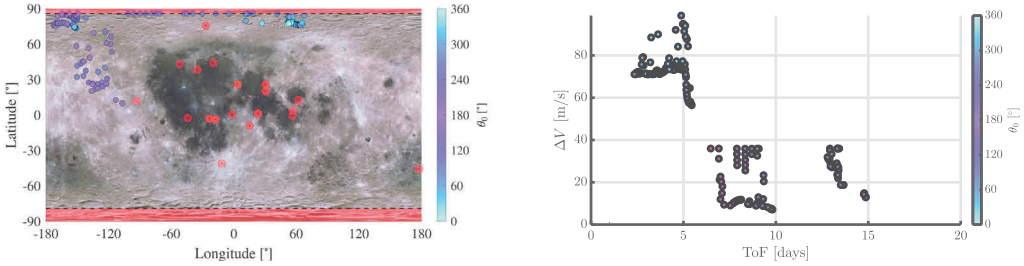

Fig. 20. Left: impact locations on the Moon surface as a function of the departure phase angle θ_0. Right: evolution of the disposal ΔV as a function of the ToF and the departure phase angle θ_0 - Orbit A1.

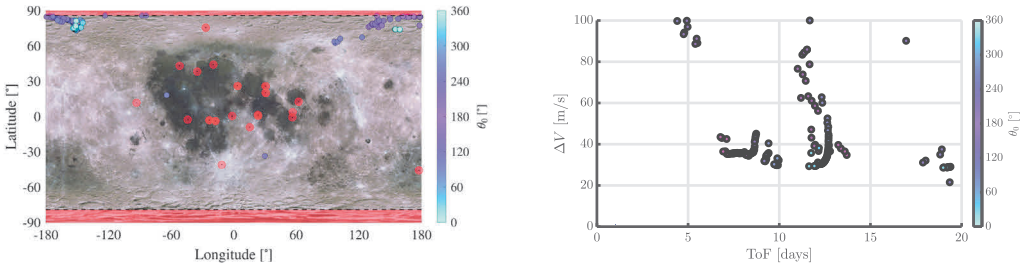

Fig. 21. Left: impact locations on the Moon surface as a function of the departure phase angle θ_0. Right: evolution of the disposal ΔV as a function of the ToF and the departure phase angle θ_0 - Orbit B1.

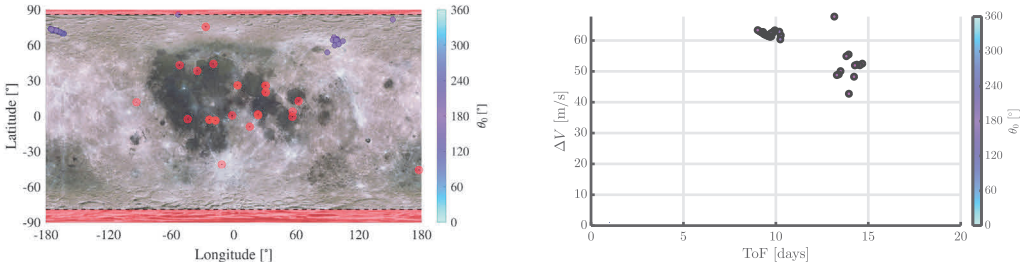

Fig. 22. Left: impact locations on the Moon surface as a function of the departure phase angle θ_0. Right: evolution of the disposal ΔV as a function of the ToF and the departure phase angle θ_0 - Orbit C1.

with mean ΔV of about 10 m/s and mean ToF of about 8 days, the second with mean ΔV of about 70 m/s and mean ToF of about 4 days. In Figs. 21 and 22, the same results are shown for B1 and C1, respectively.

Similar considerations to those discussed for B2 and C2 apply here. The solutions associated with B1 exhibit mean ΔV and ToF values comparable to those obtained for B2, while those related to C1 display a mean ΔV of approximately 55 m/s for a mean ToF of about 12 days.

Once all the simulations within the EM-CR3BP framework had been completed, the disposal trajectories identified were refined using the ephemeris-based dynamical model. The problem in the ephemeris-based dynamics is formulated in the same way as in the EM-CR3BP model, with the only difference being the required coordinate and scaling transformations that allow switching between the rotating EM frame and the J2000 reference frame, and vice versa. If the optimisation in the ephemeris-based model was unsuccessful in the preceding iteration, the solutions obtained from the EM-CR3BP dynamics are used as initial values for this second analysis. On the other hand, if the optimisation was successful, the solution obtained from the ephemeris-based dynamics is used as the initial guess, as in classical numerical continuation methods. The resulting trajectories are compared with the corresponding solutions obtained under the approximated dynamics, providing a preliminary assessment of the relationship between the two models over a limited set of cases. In Fig. 23, lunar impact disposal trajectories are shown when computed in the ephemeris-based dynamics for orbit A2, in two different views.

Generally, the ephemeris-based dynamical model exhibits a slightly lower convergence rate than the EM-CR3BP dynamics. It should be noted that, as in the previous analyses, the departure date is fixed. This represents a significant limitation from an optimisation standpoint when using the ephemeris-based model, since the departure epoch strongly influences the outcome of the disposal design. A dedicated analysis of how this parameter affects the results will be carried out in future work.

The overall trajectory profile does not completely diverge from what was obtained in the EM-CR3BP model. A notable difference, for instance, is that, with the ephemeris-based dynamics, the third manoeuvre occurs directly at the Moon for some of the options considered, which corresponds to a manoeuvre ΔV and a ToF equal to zero for the third disposal trajectory leg. The first manoeuvre is instead almost always located close to the reference periodic orbit, similarly to what was observed in the EM-CR3BP dynamics. Fig. 24 reports the resulting impact locations, along with the evolution of ΔV versus ToF.

Scatter dots identify conditions obtained under the EM-CR3BP model, whereas those derived from the ephemeris-based dynamics are

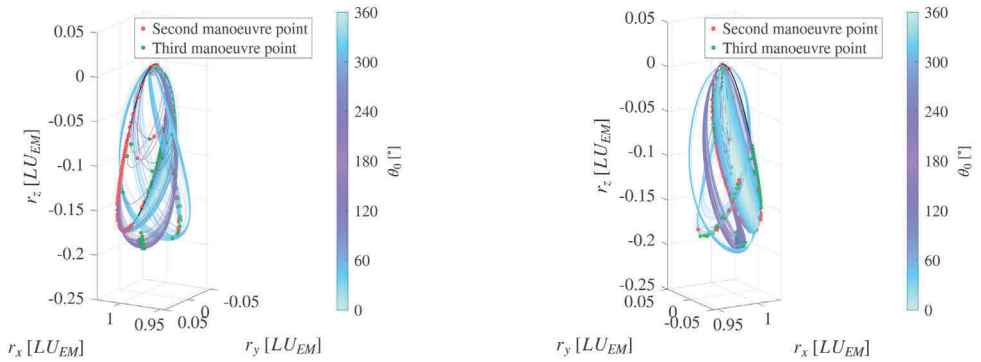

Fig. 23. Evolution of controlled lunar impact disposal trajectories, shown in two different views — Orbit A2.

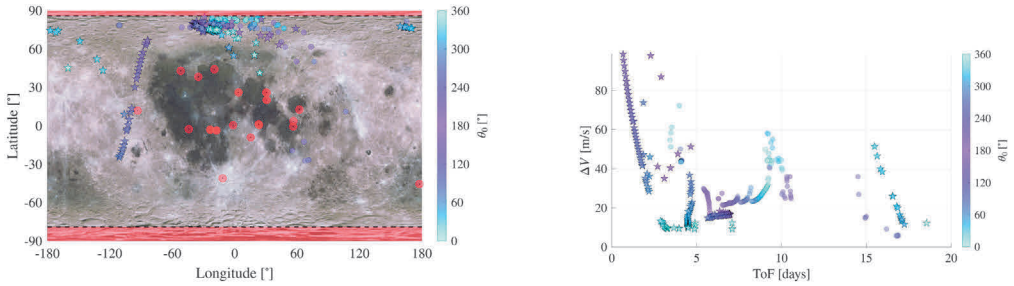

Fig. 24. Left: impact locations on the Moon surface as a function of the departure phase angle θ_0, CR3BP dynamics (dots) and ephemeris-based dynamics (stars). Right: evolution of the disposal ΔV as a function of the ToF and the departure phase angle θ_0, CR3BP dynamics (dots) and ephemeris-based dynamics (stars) - Orbit A2.

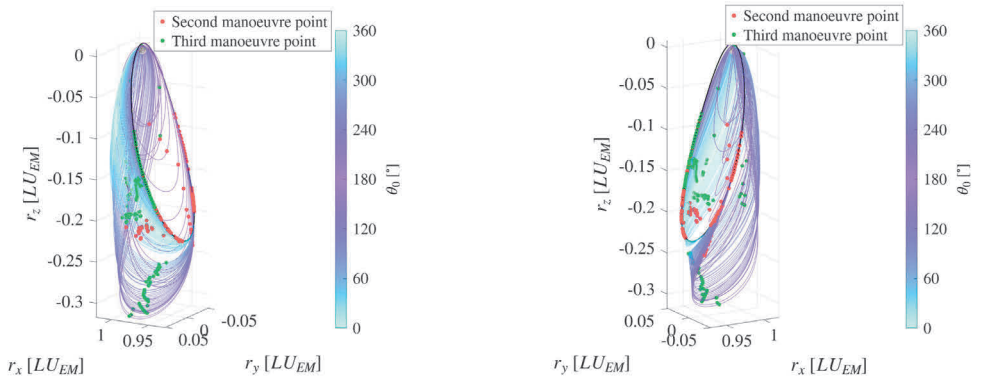

Fig. 25. Evolution of controlled lunar impact disposal trajectories, shown in two different views — Orbit A1.

marked with stars, to enable a quick and direct comparison between the results of the two models. A significant number of impact locations obtained with the ephemeris-based dynamics tend to cluster in the same region as those found using the EM-CR3BP dynamics. The consistency in latitude is due to the fact that, in both cases, the trajectory design strategy relies on a gradual lowering of the perilune. It is interesting to note, however, that in this latter case the range of latitudes covered by the impact points is much broader, and it almost appears that distinct groups of trajectories can be clearly identified, each characterised by a similar dynamical behaviour, as already partially visible in Fig. 23. The plot of the evolution of ΔV versus ToF mimics the results found for the EM-CR3BP, but it is important to highlight at least two aspects. First, when considering orbit A2, the ΔV required to dispose of the spacecraft when using ephemeris-based dynamics is generally lower than that needed for trajectories with the same departure phase angle in the EM-CR3BP model, although this does not hold for all the identified solutions. A similar trend is also observed for the ToF, as promising disposal solutions can be achieved with ΔV values of approximately 12–15 m/s and corresponding ToFs of about 4 – 5 days. Therefore, it is reasonable to conclude that controlled lunar impact disposal could be achieved with lower ΔVs and shorter ToFs than predicted using the EM-CR3BP when considering EM-L_2 NRHOs close to the Moon. Second, it is also possible in this case to identify multiple families of solutions, which form different portions of distinct Pareto fronts. This behaviour was already observed when using the EM-CR3BP dynamics, but it remains noteworthy, as it represents a clear indication of the non-linearity of the underlying dynamics. Such non-linearity favours the presence of multiple local families of solutions when varying the design parameters, rather than a single well-defined global optimum. Results relative to orbit A1 are shown in Figs. 25 and 26.

The same comments made with respect to A2 can generally be applied. It is interesting to note that, in this case, the disposal trajectories reach very high apolune altitudes before impact, likely as a result of the Sun's perturbing influence. An interesting aspect that could be explored in future work is whether more favourable disposal conditions might be achieved by deliberately exploiting the effects of the Sun

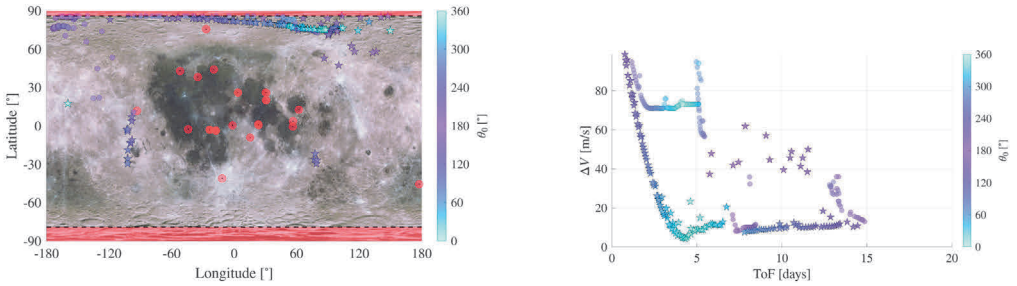

Fig. 26. Left: impact locations on the Moon surface as a function of the departure phase angle θ_0, CR3BP dynamics (dots) and ephemeris-based dynamics (stars). Right: evolution of the disposal ΔV as a function of the ToF and the departure phase angle θ_0, CR3BP dynamics (dots) and ephemeris-based dynamics (stars) - Orbit A1.

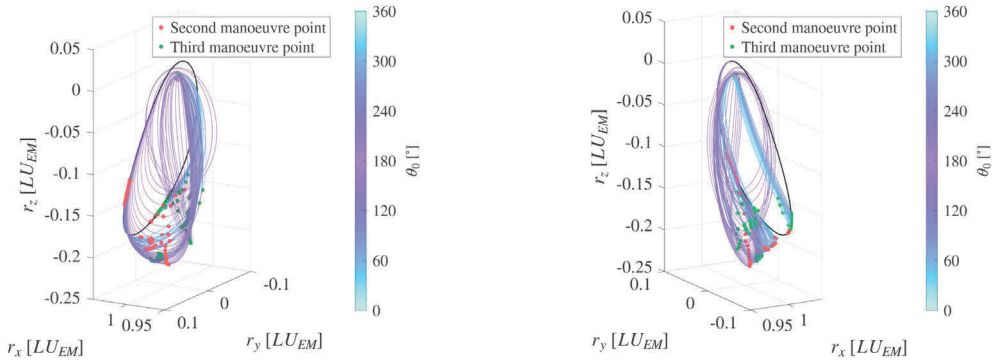

Fig. 27. Evolution of controlled lunar impact disposal trajectories, shown in two different views — Orbit B2.

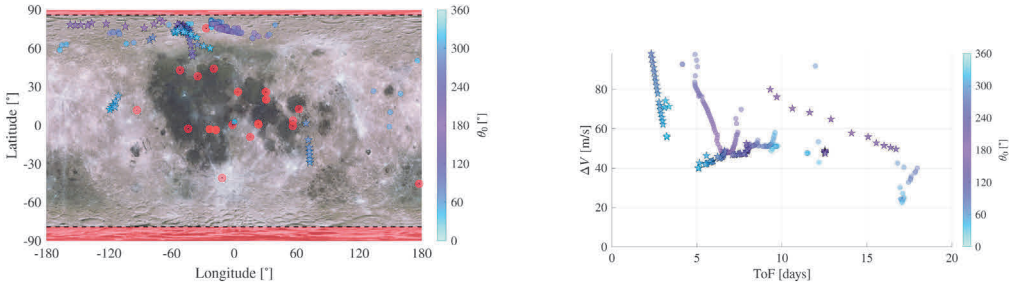

Fig. 28. Left: impact locations on the Moon surface as a function of the departure phase angle θ_0, CR3BP dynamics (dots) and ephemeris-based dynamics (stars). Right: evolution of the disposal ΔV as a function of the ToF and the departure phase angle θ_0, CR3BP dynamics (dots) and ephemeris-based dynamics (stars) - Orbit B2.

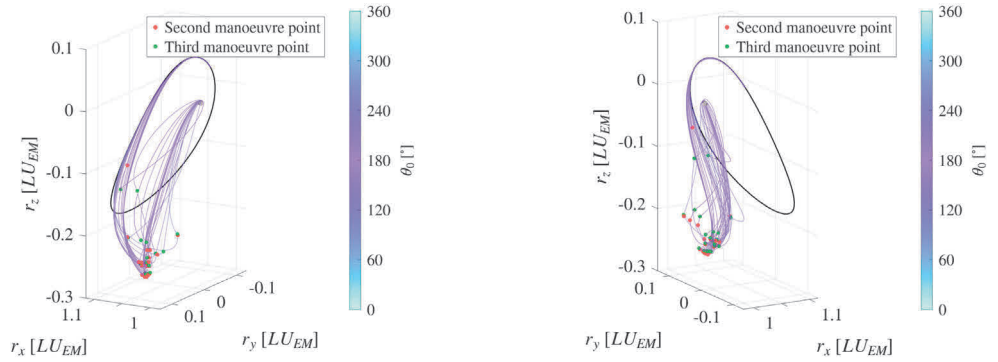

Fig. 29. Evolution of controlled lunar impact disposal trajectories, shown in two different views — Orbit C2.

and lunar gravitational harmonics. Disposal solutions for this orbit are obtained for ΔV values below 5 m/s, with ToFs of approximately 4 days. This behaviour is again attributable to the fact that some manifold trajectories associated with this orbit naturally impact the Moon, as already highlighted previously. It is therefore noteworthy to observe the consistency, in this scenario, between the simplified model and the ephemeris-based one. The results obtained in the ephemeris-based dynamics for orbits B2, C2, B1 and C1 are reported in Figs. 27 to 34.

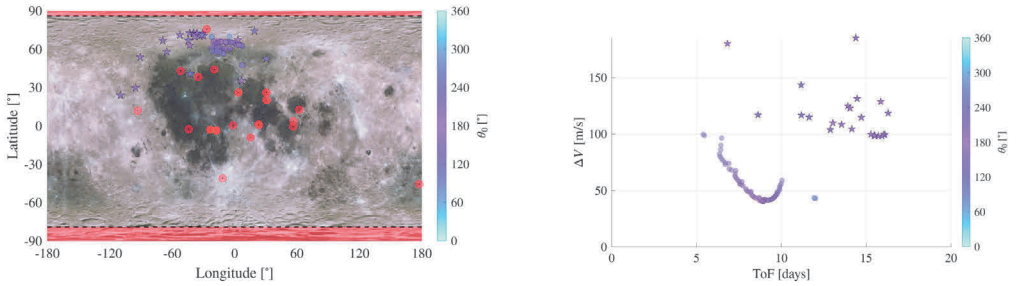

Fig. 30. Left: impact locations on the Moon surface as a function of the departure phase angle θ_0, CR3BP dynamics (dots) and ephemeris-based dynamics (stars). Right: evolution of the disposal ΔV as a function of the ToF and the departure phase angle θ_0, CR3BP dynamics (dots) and ephemeris-based dynamics (stars) - Orbit C2.

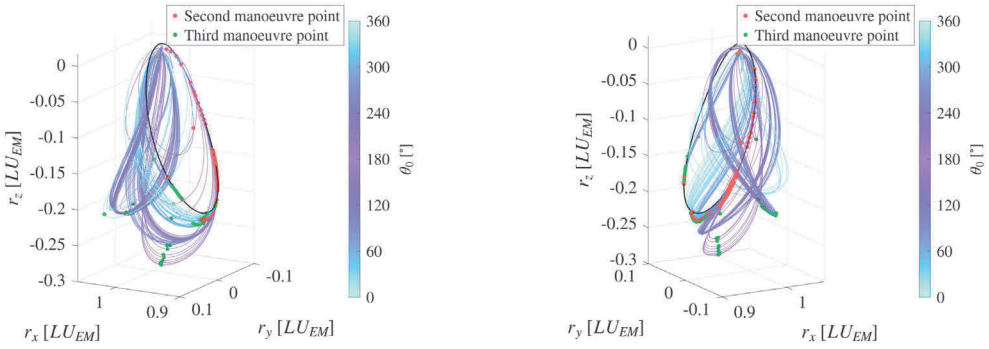

Fig. 31. Evolution of controlled lunar impact disposal trajectories, shown in two different views — Orbit B1.

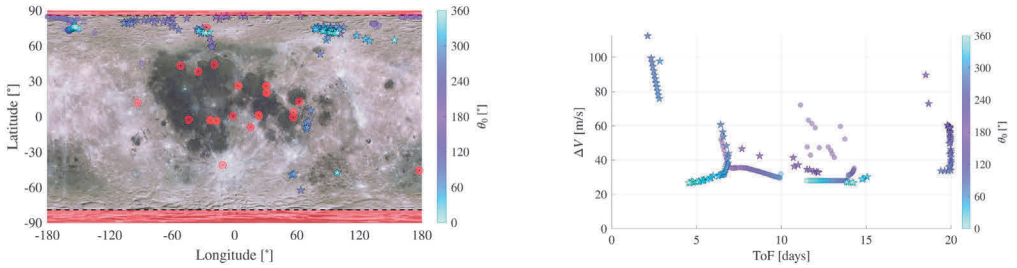

Fig. 32. Left: impact locations on the Moon surface as a function of the departure phase angle θ_0, CR3BP dynamics (dots) and ephemeris-based dynamics (stars). Right: evolution of the disposal ΔV as a function of the ToF and the departure phase angle θ_0, CR3BP dynamics (dots) and ephemeris-based dynamics (stars) - Orbit B1.

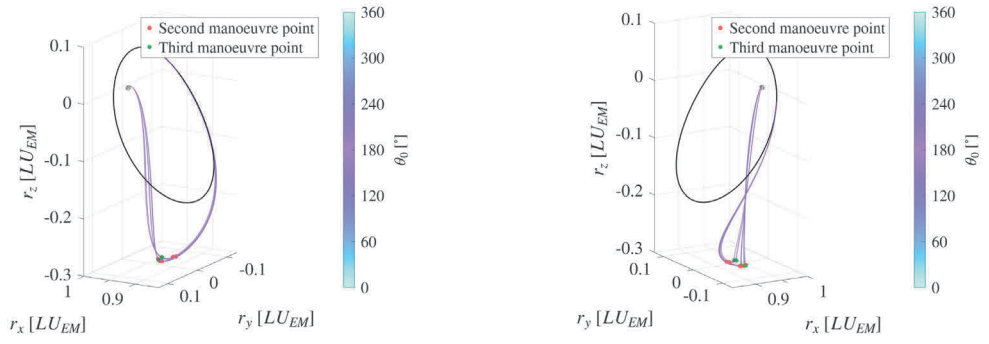

Fig. 33. Evolution of controlled lunar impact disposal trajectories, shown in two different views — Orbit C1.

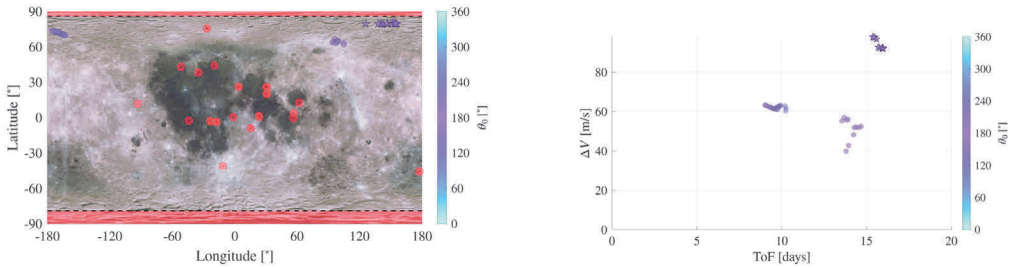

Fig. 34. Left: impact locations on the Moon surface as a function of the departure phase angle θ_0, CR3BP dynamics (dots) and ephemeris-based dynamics (stars). Right: evolution of the disposal ΔV as a function of the ToF and the departure phase angle θ_0, CR3BP dynamics (dots) and ephemeris-based dynamics (stars) - Orbit C1.

The results for B2 and B1 exhibit trends comparable to those observed for A2 and A1. A key difference, however, is that several solutions identified for B1 feature a ToF equal to the maximum allowed, 20 days, suggesting lower ΔVs could potentially be found if longer ToFs were allowed. By contrast, the outcomes for C2 and C1 are more noticeably different: they display a significantly lower convergence rate than the EM-CR3BP dynamics and are associated with higher ΔVs. This behaviour can be attributed to the previously discussed considerations for controlled lunar impact trajectories related to C2 and C1, as well as to the optimisation strategy adopted. This strategy is based on reducing the perilune of trajectories passing close to the Moon, following a path similar to the unstable manifolds of NRHOs. Consequently, while this approach is well-suited to NRHOs, it should be reconsidered for other orbital families whose manifolds naturally remain at greater distances from the Moon, as evidenced by the results obtained using the ephemeris-based model.

6. Conclusions and future works

In this work, two disposal strategies were evaluated and compared for spacecraft operating on six different LPOs: four NRHOs (two around L_1 and two around L_2) and two Halo orbits in proximity to the NRHO family. The motivation behind this study lies in the increasing interest shown in recent years towards missions targeting cislunar space, together with the need to ensure the sustainable use of space for future generations. The modelling techniques adopted for the design of both disposal strategies are first presented, followed by a detailed discussion of the corresponding results.

Despite being preliminary, this analysis made it possible to identify several key parameters that govern the search for low-cost disposal solutions, also providing insight into which approach may be more suitable depending on the characteristics of the operational orbit. For heliocentric disposal, a crucial parameter is α_0, the phase between the EM and SE systems at departure. Extending the range of α_0 in future analyses may reveal different dynamical behaviours of interest and potentially lead to even lower-cost solutions. Within this framework, heliocentric disposal proved to be a viable option for some of the orbits considered, provided that a specific departure value of θ_0 can be targeted and long TOFs before the ZVCs closure manoeuvre are acceptable. In this case, total ΔV values on the order of about 50 m/s can be achieved.

For controlled lunar impact, the main parameters influencing feasibility and cost appear to be the distance from the Moon and the characteristics of the LPO unstable manifold. Controlled impact is generally achieved at a mean total cost of approximately 50 m/s in the EM-CR3BP dynamics, but with significantly shorter ToFs than in heliocentric disposal. When considering the ephemeris-based dynamics or orbits close to the Moon, it is possible to obtain even lower ΔV (5–20 m/s) and ToFs values (4–10 days). The drawback, of course, is the requirement to impact the lunar surface, with the associated implications. Future work should therefore refine the ephemeris-based analysis to assess whether it could generate additional debris, and investigate whether dedicated disposal areas, far from protected regions, can be selected based on these characteristics. At the same time, error analyses and Monte Carlo simulations would be required to assess the uncertainty and safety margins of each scenario. This would be especially important when transitioning from the preliminary design stage to the development of solutions for real mission scenarios.

Table A.2
Initial conditions related to the orbits under consideration.

Id	x_0 $[LU_{EM},\ LU_{EM}/TU_{EM}]$	T $[TU_{EM}]$
A2	x_0 = [1.02200497 0 −0.18208322 0 −0.10322015 0]	1.51087111
B2	x_0 = [1.04520645 0 −0.19449696 0 −0.14850776 0]	1.82448727
C2	x_0 = [1.11539959 0 −0.19058524 0 −0.22351553 0]	2.84174856
A1	x_0 = [0.92791029 0 −0.22350579 0 0.11315481 0]	1.81649171
B1	x_0 = [0.912681524 0 −0.20709513 0 0.154680891 0]	1.83225997
C1	x_0 = [0.85330746 0 −0.17890824 0 0.26067241 0]	2.50228288

CRediT authorship contribution statement

Mathilda Bolis: Writing – original draft, Software, Methodology, Investigation, Formal analysis, Data curation, Conceptualization. **Elisa Maria Alessi:** Writing – review & editing, Supervision, Methodology, Investigation, Conceptualization. **Camilla Colombo:** Writing – review & editing, Supervision, Methodology, Investigation, Funding acquisition, Conceptualization.

Declaration of competing interest

The authors declare that they have no known competing financial interests or personal relationships that could have appeared to influence the work reported in this paper.

Acknowledgements

This research has received funding as part of the work developed for the agreement n. 2023-37-HH.0 for the project “Attività tecnico-scientifiche di supporto a C-SSA/ISOC e simulazione di architetture di sensori per SST”, established between ASI, Italian Space Agency, and POLIMI, Politecnico di Milano.

Appendix. Initial conditions for the orbits under consideration

In Table A.2, the initial conditions in the EM rotating reference frame, x_0, and the period, T, of the orbits selected as candidates for the analysis are reported.

It is important to note that, to avoid page overflow, not all the available significant digits of the initial state vector x_0 are reported. Moreover, due to the intrinsic characteristics of the CR3BP, the reproducibility of an orbit also depends on the numerical integrator used (MATLAB ode113 built-in integrator in this case) and on the associated

tolerance settings (relative tolerances set to $2.22045 \cdot 10^{-14}$ and absolute tolerances to 10^{-16}). As a result, the initial conditions reported above, if simply propagated within the CR3BP, will almost always not directly yield a periodic orbit. However, they can be effectively used as accurate initial guesses for a differential correction algorithm [12], which, within a few iterations, would converge to exact periodic solutions, even when slightly different integration settings are adopted.

References

[1] M.J. Holzinger, C.C. Chow, P. Garretson, A Primer on Cislunar Space, Tech. rep., Air Force Research Laboratory, Greene County, OH, USA, 2021.

[2] Artemis mission - NASA, 2026, https://www.nasa.gov/humans-in-space/artemis/. Last accessed 17 February 2026.

[3] ESA's Annual Space Environment Report, Tech. rep., 2025, https://www.sdo.esoc.esa.int/environment_report/Space_Environment_Report_latest.pdf.

[4] ESA Space Debris Mitigation Requirements, Tech. rep., ESA Space Debris Mitigation Working Group, 2023, Available at: https://technology.esa.int/upload/media/ESA-Space-Debris-Mitigation-Requirements-ESSB-ST-U-007-Issue1.pdf.

[5] Z.P. Olikara, G. Gómez, J.J. Masdemont, Dynamic mechanisms for spacecraft disposal from Sun-Earth libration points, J. Guid. Control Dyn. 38 (10) (2015) 1976–1989, http://dx.doi.org/10.2514/1.G000581.

[6] C. Colombo, E.M. Alessi, W. Van der Weg, S. Soldini, F. Letizia, M. Vetrisano, M. Vasile, A. Rossi, M. Landgraf, End-of-life disposal concepts for Libration Point Orbit and Highly Elliptical Orbit missions, Acta Astronaut. 110 (2015) 298–312, http://dx.doi.org/10.1016/j.actaastro.2014.11.002.

[7] R. Armellin, M. Rasotto, P. Di Lizia, F. Renk, End-of-life disposal of libration point orbit missions: The case of Gaia, Adv. Space Res. 56 (3) (2015) 461–478, http://dx.doi.org/10.1016/j.asr.2015.03.014.

[8] D.C. Davis, K.K. Boudad, S.M. Phillips, K.C. Howell, Disposal, deployment, and debris in Near Rectilinear Halo Orbits, in: AAS/AIAA Space Flight Mechanics Meeting, Maui, Hawaii, U.S.A., 2019.

[9] K.K. Boudad, D.C. Davis, K.C. Howell, Disposal trajectories from near rectilinear halo orbits, in: AAS/AIAA Astrodynamics Specialist Conference, Snowbird, Utah, U.S.A., 2018.

[10] P. Guardabasso, D.K. Skoulidou, L. Bucci, F. Letizia, S. Lemmens, S. Lizy-Destrez, Cislunar debris mitigation: Development of a methodology to assess the sustainability of lunar missions, in: 72nd International Astronautical Congress, IAC, Dubai, United Arab Emirates, 2021.

[11] V. Szebehely, Theory of Orbit: The Restricted Problem of Three Bodies, first ed., Academic Press, New York, 1967, http://dx.doi.org/10.1016/B978-0-12-395732-0.X5001-6.

[12] W.S. Koon, M.W. Lo, J.E. Marsden, S.D. Ross, Dynamical Systems, the Three-Body Problem and Space Mission Design, Marsden Books, 2011.

[13] R. Castelli, On the Relation Between the Bicircular Model and the Coupled Circular Restricted Three-Body Problem Approximation, Springer New York, 2011, Ch. 1.

[14] G. Gómez, J. Llibre, R. Martínez, C. Simó, Station Keeping of Libration Point Orbits. ESOC Contract 5648/83/D/JS(SC), final report, in: World Scientific Monograph Series in Mathematics, European Space Agency, 2001, 1985. Reprinted as: Dynamics and Mission Design Near Libration Points Vol.1 Fundamentals: The Case of Collinear Libration Points.

[15] B. Nicolás Ávila, Invariant Manifolds and Transport in a Sun-Perturbed Earth-Moon System (Ph.D. thesis), Department of Mathematics and Computer Science, University of Barcelona, 2022, Available at: https://hdl.handle.net/2445/190643.

[16] NASA SPICE, 2026, available at: https://naif.jpl.nasa.gov/naif/aboutspice.html. Last accessed 12 February 2026.

[17] L.E. Cunningham, On the computation of the spherical harmonic terms needed during the numerical integration of the orbital motion of an artificial satellite, Celest. Mech. 2 (1970) 207–216, http://dx.doi.org/10.1007/BF01229495.

[18] O. Montenbruck, E. Gill, Satellite Orbits: Models, Methods, and Applications, Springer Nature, 2000.

[19] GRAIL Data Sets, 2026, available at: https://pds-geosciences.wustl.edu/missions/grail/default.htm. Last accessed 12 February 2026.

[20] K. Connor Howell, Three-dimensional, periodic "halo" orbits, Celest. Mech. 32 (1) (1984) 53–71, http://dx.doi.org/10.1007/BF01358403.

[21] E.M. Zimovan-Spreen, K.C. Howell, D.C. Davis, Near rectilinear halo orbits and nearby higher-period dynamical structures: orbital stability and resonance properties, Celest. Mech. Dyn. Astron. 132 (2020) http://dx.doi.org/10.1007/s10569-020-09968-2.

[22] M. Bolis, E.M. Alessi, C. Colombo, End of-life disposal parametric analysis in cislunar space: Earth-Moon L2 escape no-return trajectories, in: 9th European Conference on Space Debris, Bonn, Germany, 2025.

[23] E. Arikan, Transfer Trajectory and Operational Orbit Selection for Earth-Moon L2 Near Rectilinear Halo Orbits Through Invariant Manifolds (Master's thesis), Politecnico di Milano, 2023, Space Engineering, Supervisor: C. Colombo, Co-advisor: E. M. Alessi. Available at: https://www.politesi.polimi.it/handle/10589/208238.

[24] J. Zhang, E. Fantino, C. Du, Y. Wang, H. Dai, Optimal transfers from an Earth-Moon unstable libration point orbit to the lunar surface, Adv. Space Res. 76 (6) (2025) 3528–3547, http://dx.doi.org/10.1016/j.asr.2025.06.072.

[25] NASA's recommendations to space-faring entities: How to protect and preserve the historic and scientific value of U.S. Government lunar artifacts, 2011, Authored by Human Exploration and operations mission directorate strategic analysis and Integration Division NASA Headquarters.

[26] Lunar reconnaissance orbiter camera, 2026, Available at: https://lroc.im-ldi.com/featured_sites. Last accessed 12 February 2026.

[27] COSPAR policy on planetary protection, 2021, Authored by COSPAR Panel on Planetary Protection and approved by the COSPAR Bureau.

[28] P. Seidelmann, V. Abalakin, M. Bursa, M. Davies, C.d. Bergh, J. Lieske, J. Oberst, J. Simon, E. Standish, P. Stooke, P. Thomas, Report of the IAU/IAG working group on cartographic coordinates and rotational elements of the planets and satellites: 2000, Celest. Mech. Dyn. Astron. 82 (2002) 83–111, http://dx.doi.org/10.1023/A:1013939327465.